Pergamon

Geochimica et Cosmochimica Acta, Vol. 66, No. 15, pp. 2639–2663, 2002

0016-7037/02 $22.00 + .00

PII S0016-7037(02)00869-4

Structure of heavy metal sorbed birnessite. Part III: Results from powder and polarized extended X-ray absorption fine structure spectroscopy

ALAIN MANCEAU,[1] BRUNO LANSON[1,*] and VICTOR A. DRITS[1,2]

[1]Environmental Geochemistry Group, LGIT, University J. Fourier, BP 53, 38041 Grenoble Cedex 9, France
[2]Geological Institute, Russian Academy of Sciences, 7 Pyzhevsky Street, 109017 Moscow, Russia

(*Received September* 18, 2001; *accepted in revised form February* 15, 2002)

Abstract—The local structures of divalent Zn, Cu, and Pb sorbed on the phyllomanganate birnessite (Bi) have been studied by powder and polarized extended X-ray absorption fine structure (EXAFS) spectroscopy. Metal-sorbed birnessites (MeBi) were prepared at different surface coverages by equilibrating at pH 4 a Na-exchanged buserite (NaBu) suspension with the desired aqueous metal. Me/Mn atomic ratios were varied from 0.2% to 12.8% in ZnBi and 0.1 to 5.8% in PbBi. The ratio was equal to 15.6% in CuBi. All cations sorbed in interlayers on well-defined crystallographic sites, without evidence for sorption on layer edges or surface precipitation. Zn sorbed on the face of vacant layer octahedral sites (□), and shared three layer oxygens (O_{layer}) with three-layer Mn atoms (Mn_{layer}), thereby forming a tridentate corner-sharing (TC) interlayer complex (Zn-3O_{layer}-□-3Mn_{layer}). ^{TC}Zn complexes replace interlayer Mn^{2+} (Mn^{2+}_{inter}) and protons. ^{TC}Zn and $^{TC}Mn^{3+}_{inter}$ together balance the layer charge deficit originating from Mn^{4+}_{layer} vacancies, which amounts to 0.67 charge per total Mn according to the structural formula of hexagonal birnessite (HBi) at pH 4. At low surface coverage, zinc is tetrahedrally coordinated to three O_{layer} and one water molecule ($^{[IV]}$TC complex: (H_2O)-$^{[IV]}$Zn-3O_{layer}). At high loading, zinc is predominantly octahedrally coordinated to three O_{layer} and to three interlayer water molecules ($^{[VI]}$TC complex: 3(H_2O)-$^{[VI]}$Zn-3O_{layer}), as in chalcophanite ($^{[VI]}ZnMn_3{}^{4+}O_7{\cdot}3H_2O$). Sorbed Zn induces the translation of octahedral layers from $-a/3$ to $+a/3$, and this new stacking mode allows strong H bonds to form between the $^{[IV]}$Zn complex on one side of the interlayer and oxygen atoms of the next Mn layer (O_{next}): O_{next}…(H_2O)-$^{[IV]}$Zn-3O_{layer}. Empirical bond valence calculations show that O_{layer} and O_{next} are strongly undersaturated, and that $^{[IV]}$Zn provides better local charge compensation than $^{[VI]}$Zn. The strong undersaturation of O_{layer} and O_{next} results not only from $Mn_{layer}{}^{4+}$ vacancies, but also from Mn^{3+} for Mn^{4+} layer substitutions amounting to 0.11 charge per total Mn in HBi. As a consequence, $^{[IV]}$Zn,Mn^{3+}_{layer}, and Mn^{3+}_{next} form three-dimensional (3D) domains, which coexist with chalcophanite-like particles detected by electron diffraction. Cu^{2+} forms a Jahn-Teller distorted $^{[VI]}$TC interlayer complex formed of two oxygen atoms and two water molecules in the equatorial plane, and one oxygen and one water molecule in the axial direction. Sorbed Pb^{2+} is not oxidized to Pb^{4+} and forms predominantly $^{[VI]}$TC interlayer complexes. EXAFS spectroscopy is also consistent with the formation of tridentate edge-sharing ($^{[VI]}$TE) interlayer complexes (Pb-3O_{layer}-3Mn), as in quenselite ($Pb^{2+}Mn^{3+}O_2OH$). Although metal cations mainly sorb to vacant sites in birnessite, similar to Zn in chalcophanite, EXAFS spectra of MeBi systematically have a noticeably reduced amplitude. This higher short-range structural disorder of interlayer Me species primarily originates from the presence of Mn^{3+}_{layer}, which is responsible for the formation of less abundant interlayer complexes, such as $^{[IV]}$Zn TC in ZnBi and $^{[VI]}$Pb TE in PbBi.

1. INTRODUCTION

The highly defective structure and nonstoichiometry of most natural Mn-oxides and oxyhydroxides present in surface environments causes them to have unusual sorptive and redox capacities for metal and organic ions (Jenne, 1967; Usui, 1979; Taylor et al., 1983; Huang, 1991). Determining the nature of surface reactive sites and binding mechanisms of trace elements associated with these minerals helps provide a solid scientific basis to modeling the fate of chemicals in the environment. Manganese minerals of the phyllomanganate group are the most common at Earth's surface and have been reported from environments as diverse as deep-ocean floors, lake sediments, and deserts (Dixon and Skinner, 1992; Post, 1999). In this group, birnessite is of uppermost importance because of its widespread occurrence in soils and sediments (Taylor et al., 1964; Ross et al., 1976; Glover, 1977; Bardossy and Brindley, 1978; Giovanoli, 1980; Chukhrov and Gorshkov, 1981; Uzochukwu and Dixon, 1986).

The structural building block of all phyllomanganates is the brucite-type layer of edge-sharing Mn octahedra. Each octahedral site is filled by tetravalent Mn cations and each anion position by oxygen atoms, resulting in the ideal composition MnO_2. This ideal structural unit has never been observed; instead, Mn layers always have a negative charge originating from Mn vacancies ($□_{Mn}$), the replacement of Mn^{4+} by Mn^{3+} (and to a lesser extent by Mn^{2+}), and, in most natural compounds, from various heterovalent cation substitutions, such as Co^{3+} for Mn^{4+} (Burns, 1976; Dillard et al., 1982; Manceau et al., 1997). The compensation mechanism of the negative charge deficiency also varies and can be achieved by the uptake of protons (OH for O substitutions) or any alkali, alkaline earth, and transition metal cations in the interlayer space between two

* Author to whom correspondence should be addressed (Alain.Manceau@ujf-grenoble.fr).

successive Mn layers. The structural environment of K, V, Cr, Zn, Pb, or Sr sorbed or exchanged in the interlayer space of phyllomanganates has been examined previously by extended X-ray absorption fine structure (EXAFS) spectroscopy, and often it has been reported that cations are connected to vacant octahedra in the Mn layer (Strobel et al., 1993; Silvester et al., 1997; Ma et al., 1999; Axe et al., 2000; Leroux et al., 2001).

This third article in the series has two objectives. The first is to complete the information obtained by X-ray diffraction (XRD, Part 1) on the average crystallographic structure of metal-sorbed birnessite, and by selected-area electron diffraction (SAED, Part 2) on the structure of the interlayer space. The symmetry and dimension of the subcell, the average atomic positions of anions and cations in the subcell, and the nature of defects, including the site occupancy of layer and interlayer cations and the nature of stacking faults, were determined from the simulation of XRD patterns. However, because the intensity of diffracted X-rays is a function of the average electronic density at each atomic position, and as a result of the simultaneous presence of manganese and sorbed metal in the interlayer region of birnessite, powder XRD has no (Zn), or moderate (Pb), sensitivity to the amount and crystallographic position of cationic species. In addition, neither of the two diffraction-based techniques allows precise probing of the coordination geometry, bonding, and local structure of sorbed cations, especially at low sorbate concentration. Owing to its chemical selectivity at even low metal concentration, EXAFS spectroscopy coupled with empirical bond valence calculations offer complementary clues to the structure of the series of metal-sorbed birnessite samples examined in the two companion articles. One of the principal findings of this study is the firm evidence for the formation of tetrahedrally coordinated Zn complexes at low surface coverage as a direct result of the presence of Mn^{3+} in the birnessite layers. This information was used to constrain XRD simulations in Part 1 and to determine more realistic structural formulas. The second purpose of this article is to generate an EXAFS database of a well-characterized series of metal-sorbed birnessites, against which EXAFS data obtained on natural Mn oxides containing metallic elements can be compared in future studies.

2. CRYSTAL STRUCTURE OF PHYLLOMANGANATES

Complete characterization of the 3D structure of three phyllomanganates, quenselite (Rouse, 1971), chalcophanite (Wadsley, 1955; Post and Appleman, 1988), and hexagonal birnessite (Chukhrov et al., 1985; Silvester et al., 1997; Lanson et al., 2000) has been obtained previously by XRD. In this article, multiple references are made to these three benchmark phyllomanganates for interpreting EXAFS results, and for clarity, their structures are presented below.

Quenselite, ideally $PbMnO_2OH$, has a structure composed of a series of sheets with the sequence Mn-O- (Pb,OH)-(OH,Pb)-O-Mn. All octahedral positions of the MnO_2 layer are filled by Mn^{3+} cations (Fig. 1). The negative layer charge is balanced by interlayer Pb^{2+}. Lead is coordinated to three oxygen atoms of the MnO_2 layer (O_{layer}, bond lengths 2.22, 2.99, 3.16 Å) and to three interlayer OH groups (O_{inter}, bond lengths 2.31, 2.37, 2.76 Å). It fills a tetrahedral hole above O_{layer}, and therefore its polyhedron shares three edges with the underlying Mn octahedra (tridentate edge-sharing interlayer complex, or TE). As expected from its electronic structure, divalent lead is off center in its coordination polyhedron owing to the presence of a stereoactive lone pair of $6s^2$ electrons (e.g., Hyde and Anderson, 1989). For electrostatic reasons, the lone pair is directed toward the two distant oxygen atoms at 2.99 and 3.16 Å. As a consequence, O_{inter} forms two sheets, each nearly coplanar with Pb, and the lead atom is eccentric in the tetrahedral site, forming one strong bond ($d(Pb\text{-}O_{layer}) = 2.22$ Å) and two weak bonds ($d(Pb\text{-}O_{layer}) = 2.99$ and 3.16 Å) with the manganese layer. Similar to the Pb-(O,OH) distances, the Pb-Mn distances are unequal (3.43, 3.58, 3.96 Å).

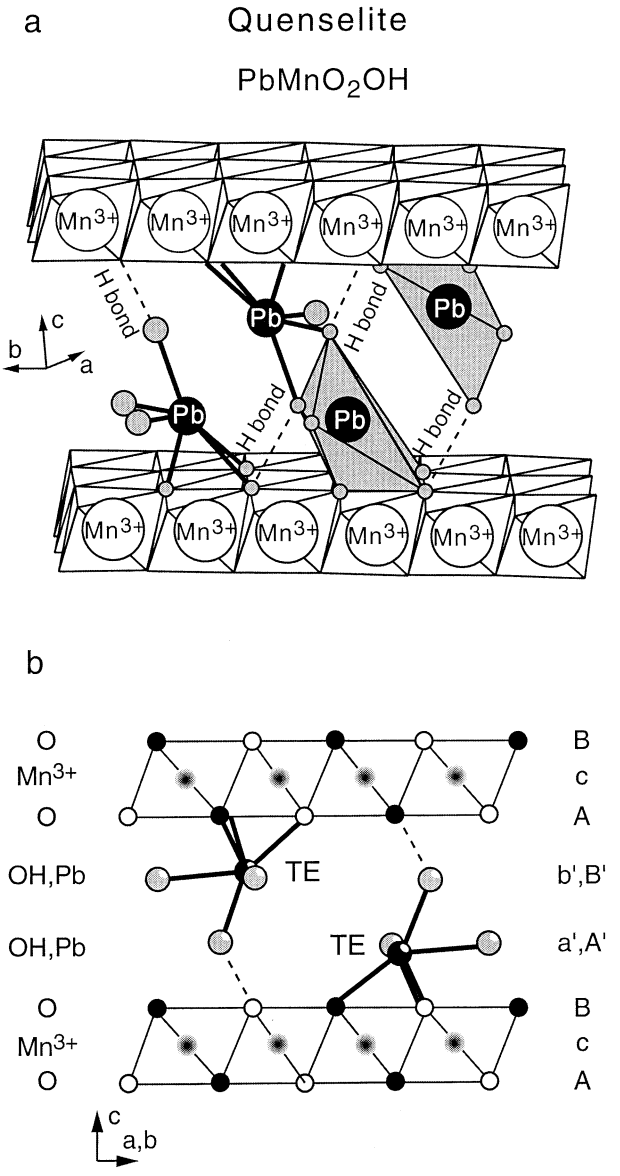

Fig. 1. Polyhedral representation (a), and composition of anionic and cationic sheets, stacking mode, and interlayer structure (b) of quenselite. After Rouse (1971).

Chalcophanite, ideally $ZnMn_3O_7 \cdot 3H_2O$, has the following sheet sequence parallel to (001): Mn-O-Zn-H_2O-Zn-O-Mn (Fig. 2). Successive Mn layers are translated by $+a/3$, and they

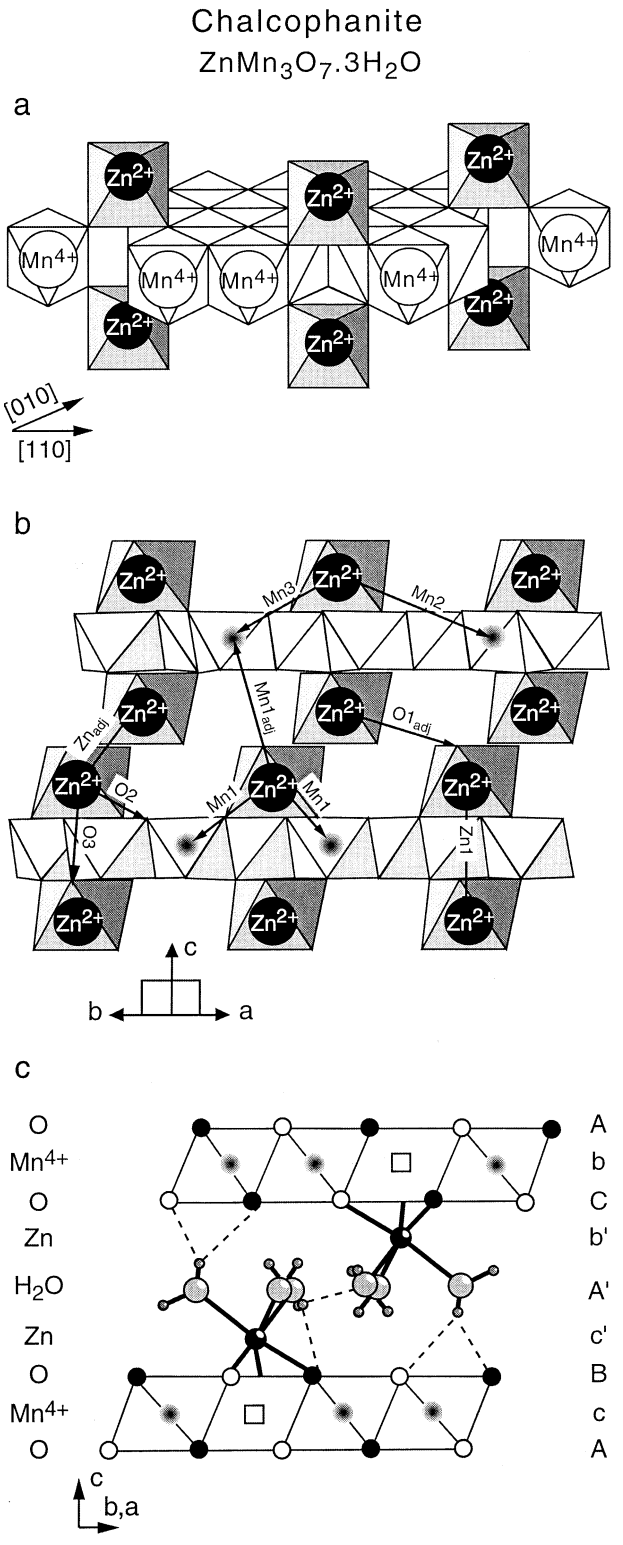

Fig. 2. Polyhedral representation (a, b), and composition of anionic and cationic sheets, stacking mode, and interlayer structure (c) of chalcophanite. Squares are vacant layer sites. In (b), bond numbering are used in explaining EXAFS data. After Wadsley (1955) and Post and Appleman (1988).

have hexagonal symmetry as in an ideal stoichiometric MnO_2 layer owing to the presence of only Mn^{4+}. One in seven of the octahedral sites is vacant, and therefore, the octahedral sheet formula normalized to one vacancy can be written $[Mn_6\square_1O_{14}]^{4-}$. The 4− charge deficiency at each vacancy is perfectly compensated above and below by Zn^{2+} cations in octahedral coordination ($^{[VI]}$Zn). Each Zn is coordinated on one side to three O_{layer} (bond length 2.07 Å) and on the other side to three H_2O molecules forming an H_2O sheet (O_{inter}, bond length 2.14 Å). Consequently, each Zn octahedron fills an octahedral site above the oxygen sheet and shares three corners with layer Mn octahedra (d(Zn-Mn_{layer}) = 3.49 to 3.50 Å), thus forming a tridentate corner-sharing octahedral interlayer complex ($^{[VI]}$TC).

The sheet sequence of synthetic hexagonal birnessite (HBi) is Mn-(O,OH)-Mn-H_2O-Mn-(O,OH)-Mn and its ideal structural formula at pH 4 is $H^+_{0.333}Mn^{3+}_{0.123}Mn^{2+}_{0.043}(Mn^{4+}_{0.722}Mn^{3+}_{0.111}\square_{0.167})(OH)_{0.013}O_2 \cdot 0.48H_2O$, where cations within the parentheses are in the layer and those outside are in the interlayer (Fig. 3). The layer charge now arises from Mn vacancies and Mn^{3+} for Mn^{4+} substitutions and is compensated by protons and interlayer Mn^{2+} and Mn^{3+} cations, the relative proportions of which vary with pH. About one-sixth of Mn layer sites are vacant, and each octahedral hole is capped by one interlayer Mn^{2+} or Mn^{3+}. Structural studies by X-ray and electron diffraction and by EXAFS spectroscopy showed that hydrolyzable cations, such as Zn, Cd, and Pb, can be taken up in the interlayer to form TC complexes (Zn, Cd, Pb), and at high surface loading TE (Pb), complexes (Silvester et al., 1997; Matocha et al., 2001; Drits et al., 2002; Lanson et al., 2002a). Hexagonal birnessite is the low-pH modification of triclinic birnessite (TcBi) synthesized in alkaline conditions from the topotactic transformation of $Mn(OH)_2$ to $Na_{0.30}Mn^{2+}_{0.05}(Mn^{4+}_{0.74}Mn^{3+}_{0.21}\square_{0.05})O_{\sim 2}$ in the presence of oxygen (Silvester et al., 1997; Lanson et al., 2002b). In TcBi, all octahedral layer positions are filled with Mn^{4+} and Mn^{3+} cations, and Mn^{3+} forms rows in the b direction alternating along the a direction with two Mn^{4+} rows (3a superstructure motif, Fig. 3c; Drits et al., 1997). The TcBi to HBi transformation proceeds by the disproportionation of 0.1 layer Mn^{3+} per Mn octahedral site according to the reaction: $2Mn^{3+}_{layer} \rightarrow Mn^{4+}_{layer} + Mn^{2+}_{layer} \rightarrow Mn^{4+}_{layer} + \square + Mn^{2+}_{aq}$, followed by the migration of about one half of the remaining layer Mn^{3+} atoms to the interlayer space on either side of the newly formed vacancies. At equilibrium, the disproportionation and migration reactions result in a 50% occupancy of layer cation positions along the former Mn^{3+}-rich rows. Because these rows alternate with two successive Mn^{4+} rows, the proportion of octahedral holes, and interlayer cations above or below them is 0.5/3 = 0.167, in agreement with the ideal structural formula of HBi. Successive Mn layers are translated by $-a/3$ in TcBi and superimposed without layer displacement in HBi. They are held together by hydrogen bonds.

3. MATERIALS AND METHODS

3.1. Samples

Preparation conditions of metal sorbed birnessite (MeBi) were described in Part 1 (Lanson et al., 2002a). Samples examined by EXAFS encompass those from the ZnBi (ZnBi 8, ZnBi 69, ZnBi 128), PbBi

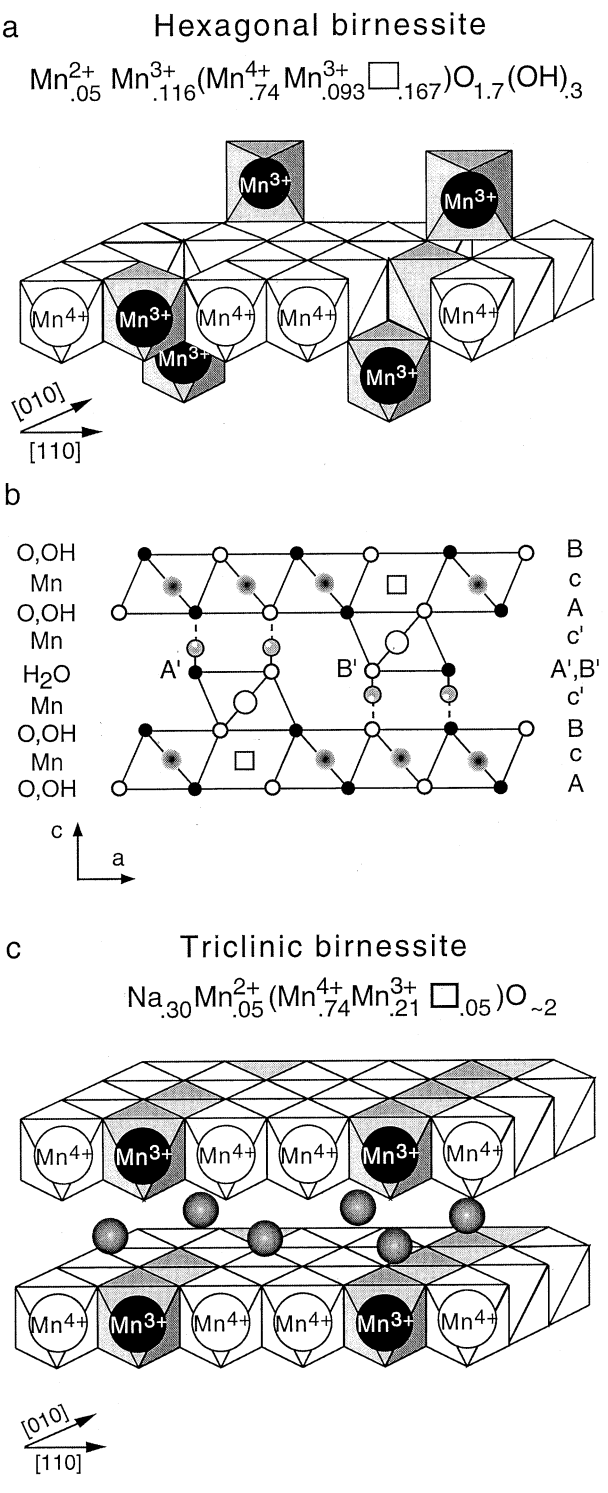

Fig. 3. Polyhedral representation (a) and composition of anionic and cationic sheets, stacking mode, and interlayer structure (b) of hexagonal birnessite. Squares are vacant layer sites. (c) Polyhedral representation of triclinic birnessite. After Silvester et al. (1997) and Lanson et al. (2000, 2002b).

(PbBi 6, PbBi 58), and CuBi (CuBi 156) series, previously studied by X-ray and electron diffraction, and include two new ones, PbBi 1 and PbBi 31. PbBi 1 was synthesized to compare the structure of Pb sorption complexes at low and intermediate surface loading, and PbBi 31 was synthesized to fill in the concentration gap between PbBi 6 and PbBi 58. The number that follows the MeBi denomination corresponds to the Me/Mn atomic ratio times 1000 in the bulk solid, as determined by chemical analysis. The interlayer has a different Me/Mn ratio because, according to XRD (Lanson et al., 2002a), it contains both Me and Mn^{3+} cations, whereas the layer contains only Mn^{3+} and Mn^{4+} cations.

3.2. Powder and Polarized EXAFS Spectroscopy

3.2.1. Data Acquisition

EXAFS measurements of concentrated samples (MeBi with Me/Mn >20) were performed on the D42 spectrometer at the Laboratoire pour l'Utilisation du Rayonnement Electromagnetique (LURE, Orsay, France). Spectra were recorded in transmission mode with gas ionization chambers filled with an air/helium mixture adjusted to attenuate the beam intensity by ~20% before and ~50% after sample entry. Spectra of diluted samples were recorded in fluorescence-yield detection mode at the European Synchrotron Radiation Facility (ESRF, Grenoble, France) on the D32 CRG/IF beamline. A multielement Ge solid-state detector was used to select the $K\alpha$ (Cu, Zn) or $L\alpha$ (Pb) fluorescence of the sorbate, and to remove the $K\alpha$ Mn background fluorescence from the substrate. This undesired fluorescence is very intense and represents more than 90% of the total signal entering the detector at low sorbate concentration. Reasonably good EXAFS spectra were obtained by averaging three to five scans and by setting the counting time per point to 20 to 30 s, depending on the sample. ZnBi 69 was prepared as a self-supporting film for polarized EXAFS (P-EXAFS) measurements. P-EXAFS spectra were collected in fluorescence-yield detection mode by rotating the film preparation around an axis normal to both the beam direction and the electric field vector **E**. The angular dependence of the P-EXAFS χ function is given by (Heald and Stern, 1977; Brouder, 1990)

$$\chi(k, \alpha) = [\chi(k, \alpha = 0°) - \chi(k, \alpha = 90°)]\cos^2\alpha + \chi(k, \alpha = 90°), \quad (1)$$

where α is the angle between **E** and the layer plane. α was equal to 0°, 20°, 35°, and 50°, and the out-of-plane $\chi(k,\alpha = 90°)$ function was calculated for each k value via linear regression as a function of $\cos^2\alpha$ and extrapolation to 90° (Manceau et al., 1988, 1998). Powder EXAFS spectra were recorded at $\alpha = 35°$ to eliminate orientation effects due to the preferred orientation of birnessite platelets in powdered samples (Manceau et al., 1990).

3.2.2. Data Reduction

EXAFS spectra were analyzed according to standard procedures (Lengeler and Eisenberger, 1980). Radial structure functions (RSFs) were obtained by Fourier-transforming EXAFS spectra with a Kaiser function window (Manceau and Combes, 1988) to minimize the intensity of side lobes (i.e., harmonic peaks) resulting from truncation effects (Teo, 1986; Manceau and Combes, 1988; Manceau, 1995). RSFs were not corrected for EXAFS phase shifts, causing peaks to appear at shorter distances ($R + \Delta R$ with $\Delta R \sim -0.3$ to -0.4 Å) relative to the true near-neighbor distances (R) (Lengeler and Eisenberger, 1980). Interatomic R distances and numbers of atoms in the two nearest atomic shells (N) around the sorbed metal were determined by fitting Fourier back-transformed (FT^{-1}) RSF peaks by using experimental phase shift and amplitude functions when available, and theoretical functions otherwise. Functions for the Zn-O and Zn-Mn pairs were obtained from ZnO (d(Zn-O) = 1.98 Å, $N_O = 4$; Albertsson et al., 1989) and from chalcophanite (d(Zn-Mn) = 3.49 Å, $N_{Mn} = 6$; Post and Appleman, 1988), respectively. Functions for Cu-O, Cu-Mn, Pb-O, and Pb-Mn were calculated ab initio with the FEFF 7.02 code (Rehr et al., 1991); chalcophanite was used as a model compound after replacing Zn by Cu and Pb. The precision on R and N are typically 0.02 Å and 20% for Zn and Cu. For Pb, the precision is lower because of the wide distribution of interatomic distances systematically observed in divalent lead compounds (Manceau et al., 1996). The structural significance of Pb-EXAFS results will be discussed later. The number of floated parameters used to build model EXAFS spectra never exceeded the

number of degrees of freedom (N_{Free}) given by the Nyquist theorem $N_{Free} = (2\Delta k\ \Delta R/\pi) + 2$, where Δk is the range of the k-space fit and ΔR is the width of the FT^{-1} ($R \rightarrow k$) window (Brigham, 1974; Stern, 1993). The least squares difference between experimental and theoretical spectra was quantified by the figure of merit R_p defined as $R_p = \Sigma (k^n\chi_{exp} - k^n\chi_{th})^2/\Sigma (k^n\chi_{exp})^2$.

4. RESULTS

4.1. Zn K-Edge

4.1.1. Powder EXAFS

At high Zn concentration (ZnBi 128), the EXAFS spectrum for birnessite is similar to that of chalcophanite (ZnCh), the unknown and reference spectra differing essentially by their amplitude (Fig. 4a). With decreasing Zn concentration, the frequency of the EXAFS oscillations gradually shifts to the right and the maximum at 7.5 Å disappears (arrow in Fig. 4c). The change in spectral shape indicates that either the bonding geometry or the sorption site of Zn interlayer complexes varies with the metal concentration. The shift in frequency indicates a reduction of interatomic distances around Zn.

Three predominant peaks, labeled A, B, and C in Figure 5a, are systematically observed in all RSFs, and the imaginary parts of the Fourier transforms (FTs) for birnessite ZnBi 128 and ZnCh are almost superimposed. Clearly, at high concentration the coordinative environment of Zn is similar in the two phyllomanganates, and peaks A, B, and C can be assigned on the basis of the structure of chalcophanite (Fig. 2). Peak A (O1 shell) corresponds to the contribution from the O_{layer} and O_{inter} (i.e., H_2O) oxygen atoms coordinated to Zn, peak B (Mn1 shell) to the six nearest manganese atoms at 3.49 to 3.50 Å, and peak C (Mn2 shell) to the six next-nearest Mn at 5.38 Å (Table 1; Wadsley, 1955; Post and Appleman, 1988). The amplitude maxima and the imaginary parts of the three major RSF peaks progressively shift to lower $R + \Delta R$ values with decreasing Zn content. This reduction in distances, previously inferred from the frequency of EXAFS spectra, affects all atomic pairs.

The shortening of the average Zn-O distance with decreasing Zn content can be interpreted by the existence of two interlayer complexes, one having shorter Zn-O distance predominantly present at low surface loading (complex 1), and one having longer Zn-O distance formed at high loading (complex 2). However, the omnipresence of peaks B and C, and their gradual left-shift in parallel to peak A, suggest that Zn is similarly bonded to the birnessite surface at all coverages. The structural disorder resulting from the presence of at least two interlayer complexes, which obviously have different Zn-O and Zn-Mn distances, accounts for the systematic reduction in amplitude of EXAFS spectra and RSF peaks of sorption samples compared with chalcophanite. In sample ZnBi 128, complex 2 is overwhelmingly present, and the small, but significant, spectral differences from ZnCh arise from the residual contribution of complex 1. Therefore, the evolution of EXAFS spectra and RSFs with increasing Zn concentration affords an additional clue to the chalcophanite-like local structure of complex 2 in birnessite.

Contributions from the O1 shells were analyzed quantitatively by Fourier backtransforming the first RSF peaks in the [1.2 to 2.2] Å $R + \Delta R$ interval. All samples have a wave frequency intermediate between those of chalcophanite and

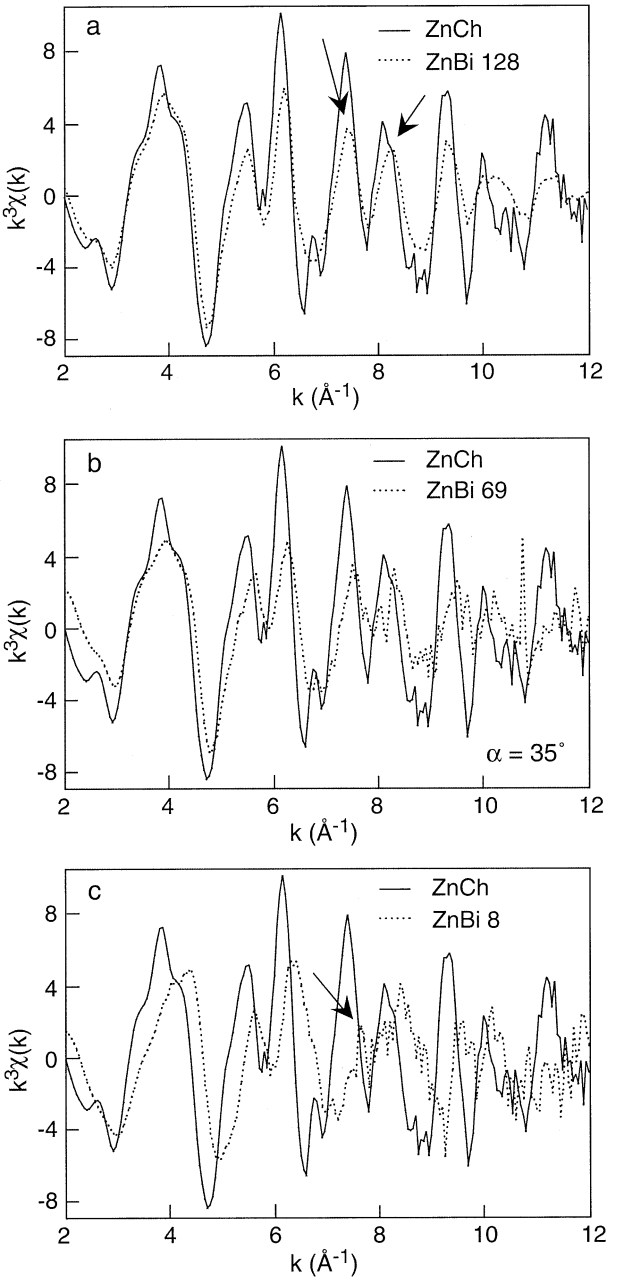

Fig. 4. Zn K-edge EXAFS spectra of Zn-sorbed birnessites compared with that of chalcophanite ($ZnMn_3O_7{\cdot}3H_2O$). At high Zn concentration (a), both spectra have a similar shape and frequency. With decreasing Zn concentration (b, c), birnessite spectra have different shapes at 8 $Å^{-1}$, and their frequencies are right-shifted. Spectral dissimilarities come from the presence of $^{[IV]}$Zn complexes at low surface coverage.

$Zn(OH)_2$ (Fig. 6a). Because Zn is six-fold coordinated ($^{[VI]}$Zn) in chalcophanite, and four-fold coordinated ($^{[IV]}$Zn) in $Zn(OH)_2$, this suggests that complex 1 corresponds to a $^{[IV]}$Zn species (complex 2 obviously corresponds to a $^{[VI]}$Zn species). This inference was confirmed by comparing linear combinations of the two reference χ_O functions to the birnessite Zn-O contributions (Fig. 6b). The unknown contributions could be reproduced by assuming the presence of 70% $^{[IV]}$Zn + 30% $^{[VI]}$Zn in ZnBi 8, 30% $^{[IV]}$Zn + 70% $^{[VI]}$Zn in ZnBi 69, and

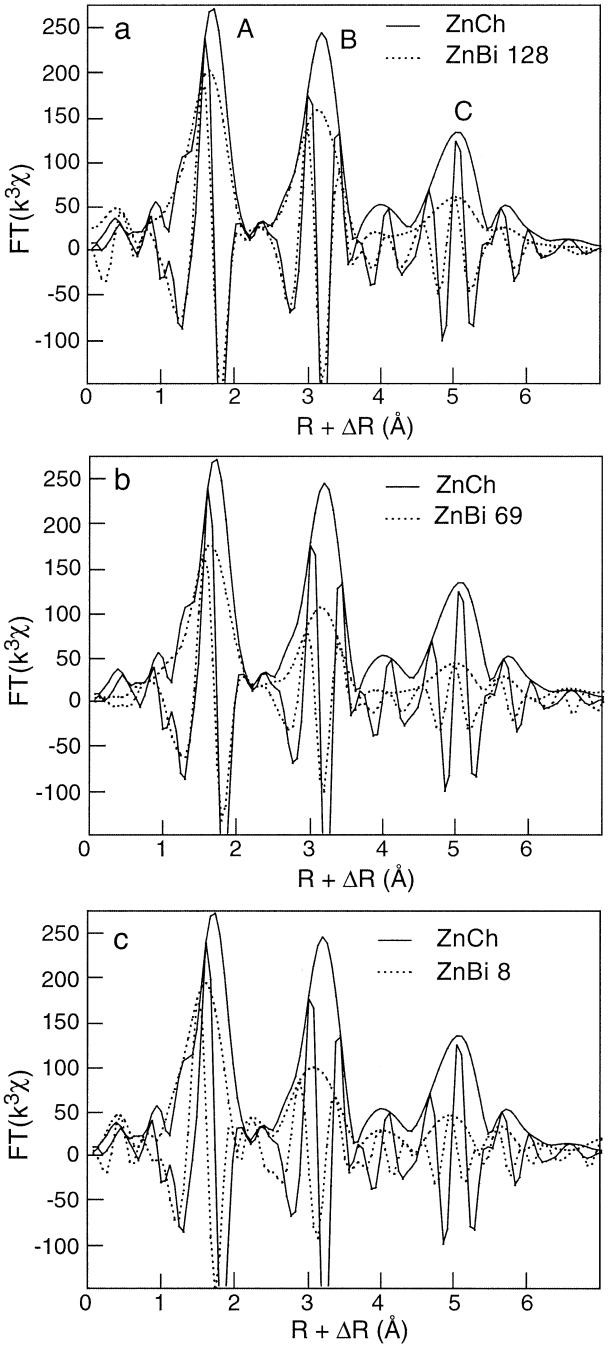

Fig. 5. Zn K-edge RSFs of Zn-sorbed birnessites compared with that of chalcophanite. The envelope curves are the magnitude of the Fourier transforms (RSF = $[Im(FT)^2 + Re(FT)^2]^{1/2}$) and the oscillatory curves are the imaginary parts of the transforms. Peaks A, B, and C, correspond, respectively, to the contribution of O1, Mn1, and Mn2 atomic shells from birnessite. The presence of the Mn1 and Mn2 shells is characteristic of tridentate corner-sharing (TC) Zn interlayer complexes above vacant layer sites. At low Zn concentration (c), the three RSF peaks are shifted to smaller distances. The shortening of all interatomic distances about Zn is consistent with the right-shift in frequency of EXAFS spectra observed in Fig. 4c and results from the presence of $^{[IV]}$Zn complexes.

Table 1. Principal atomic shells and interatomic distances from Zn in chalcophanite (after Post and Appleman, 1988).

Atomic shell	RSF peak	R (Å)	β (°)	N_{powder}	$N^{\parallel}_{polar}$	$N^{\perp}_{polar}$
O1	A	2.07–2.14	60.2–51.3	6	6.1	5.7
O2	B	3.43	71.4	3	4.0	0.9
Mn1	B	3.49–3.50	53.6	6	5.8	6.3
O3	B	3.61	29.8	3	1.1	6.8
$O1_{adj}$ [a]	B	3.69	67.1	3	3.8	1.4
Zn1	D	4.16	0	1	0	3
$O2_{adj}$	—	4.46	71.1	3	4.0	0.9
O4	—	4.47–4.51	46.8–75.9	6	6.6	4.7
$O3_{adj}$	—	4.49–4.81	75.5–35.5	9	9.1	12.3
$Mn1_{adj}$	E	5.14	19	3	0.5	8.0
Zn_{adj}	—	5.16	57.5	3	3.2	2.6
$O4_{adj}$	—	5.30	55.1	3	3.0	2.9
O	—	5.34	55	3	3.0	2.9
Mn2	C	5.38	67.5	6	7.6	2.6
$Mn2_{adj}$	—	5.85	34.2	3	1.4	6.2
Mn3	F	6.08	70.1	6	7.9	2.1

[a] Atom from adjacent layers; see Figure 2.

25% $^{[IV]}$Zn + 75% $^{[VI]}$Zn in ZnBi 128. The percentage of $^{[IV]}$Zn in ZnBi 128 is in good agreement with that obtained by XRD (28.5%, Lanson et al., 2002a).

The $k^3\chi_{O1}$ function of ZnCh displays a beat node pattern at 13.2 $Å^{-1}$ that reduces the amplitude of the wave oscillation and indicates the presence of two oxygen subshells separated by $\Delta R = \pi/(2 \times 13.2) = 0.12$ Å (Fig. 7a). The wave function was satisfactorily reproduced by assuming 3.0 $O1_1$ (O_{layer}) at 2.04 Å (σ = 0.07 Å) and 3.0 $O1_2$ (O_{inter}) at 2.16 Å (σ = 0.07 Å, $R_p = 8 \times 10^{-3}$) (Table 2). For consistency with the crystallographic structure of chalcophanite, the number of oxygen atoms in the two subshells was constrained to be identical during the fit. The two Zn-O1 EXAFS distances are similar to the XRD distances determined by Post and Appleman (1988) (3 $O1_1$ at 2.07 Å and 3 $O1_2$ at 2.14 Å) but larger than those reported in Wadsley's (1955) pioneering study (3 $O1_1$ at 1.95 to 1.99 Å and 3 $O1_2$ at 2.13 to 2.15 Å). Theoretical $k^3\chi_{Zn\text{-}O1}$ functions for the two sets of XRD values were computed and are compared with the experimental EXAFS function in Figures 7b and 7c. Post and Appleman's (1988) structural model matches fairly well the EXAFS signal below 10 $Å^{-1}$; however, the beat node pattern is shifted to higher k values ($k = \pi/(2 \times \Delta R) = 22$ $Å^{-1}$) as a result if the smaller difference between Zn-$O1_1$ and Zn-$O1_2$ distances in this model (ΔR = 0.07 Å). Also, when the Zn-$O1_1$ and Zn-$O1_2$ distances were fixed during the least squares fit to their XRD values, the Debye-Waller disorder parameter $\Delta\sigma_{O12}$ increased from 0.00 Å to 0.04 Å (Fig. 7b), indicating that Zn-$O1_2$ distances are distributed around the arbitrarily constrained 2.14 Å value. The theoretical $k^3\chi_{Zn\text{-}O1}$ wave corresponding to Wadsley's (1955) model displays a beat node pattern at $k = 9.2$ $Å^{-1}$ [$2k\Delta R = 2 \times 9.2 \times (2.14–1.97) = \pi$], which is 4 $Å^{-1}$ shifted compared with the experimental one (k = 13.2 $Å^{-1}$; Fig. 7c).

Because complex 2 has a chalcophanite-like structure, its O1 shell also is expected to be split into two subshells at ~2.04 Å and 2.16 Å. The Zn-O bond length in tetrahedral coordination

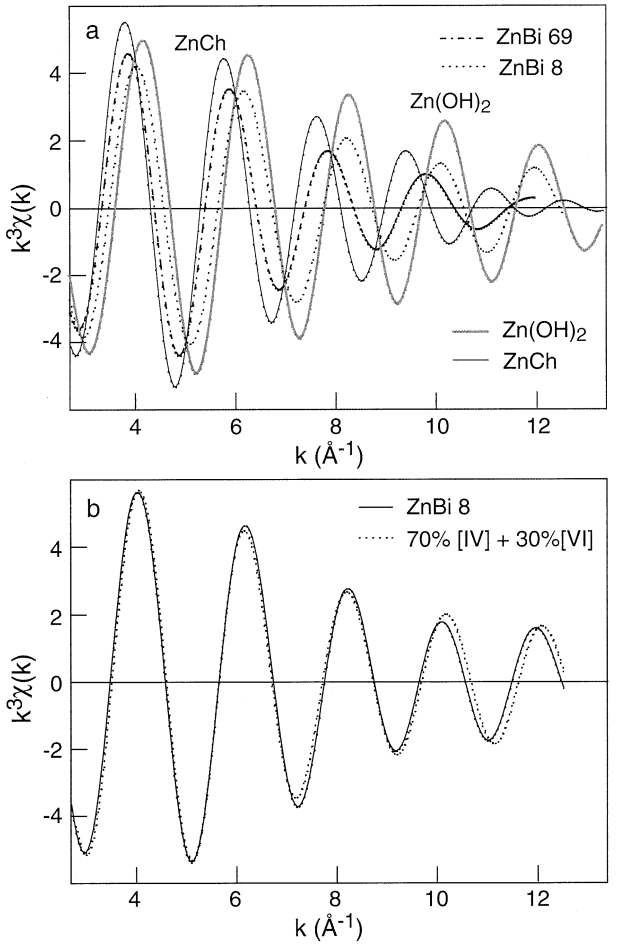

Fig. 6. (a) Comparison of Fourier filtered $k^3\chi_{\text{Zn-O1}}$ functions for Zn-sorbed birnessites (ZnBi 69 and ZnBi 8) and sixfold (chalcophanite) and fourfold ($Zn(OH)_2$) Zn-coordinated references. The $k^3\chi_{\text{Zn-O1}}$ functions represent the contribution to EXAFS spectra of the Zn-O1 pairs and were obtained by inverse Fourier transforming the first RSF peaks in Fig. 5. ZnBi 128 has a similar $k^3\chi_{\text{Zn-O1}}$ function (data not shown) to that of ZnBi 69, indicating that these two samples have a similar $^{[IV]}Zn/(^{[IV]}Zn + ^{[VI]}Zn)$ ratio. (b) The $k^3\chi_{\text{Zn-O1}}$ functions of sorption samples are linear combinations of the $^{[VI]}Zn$ and $^{[IV]}Zn$ references indicating the presence of sixfold ($^{[VI]}Zn$) and fourfold ($^{[IV]}Zn$) complexes.

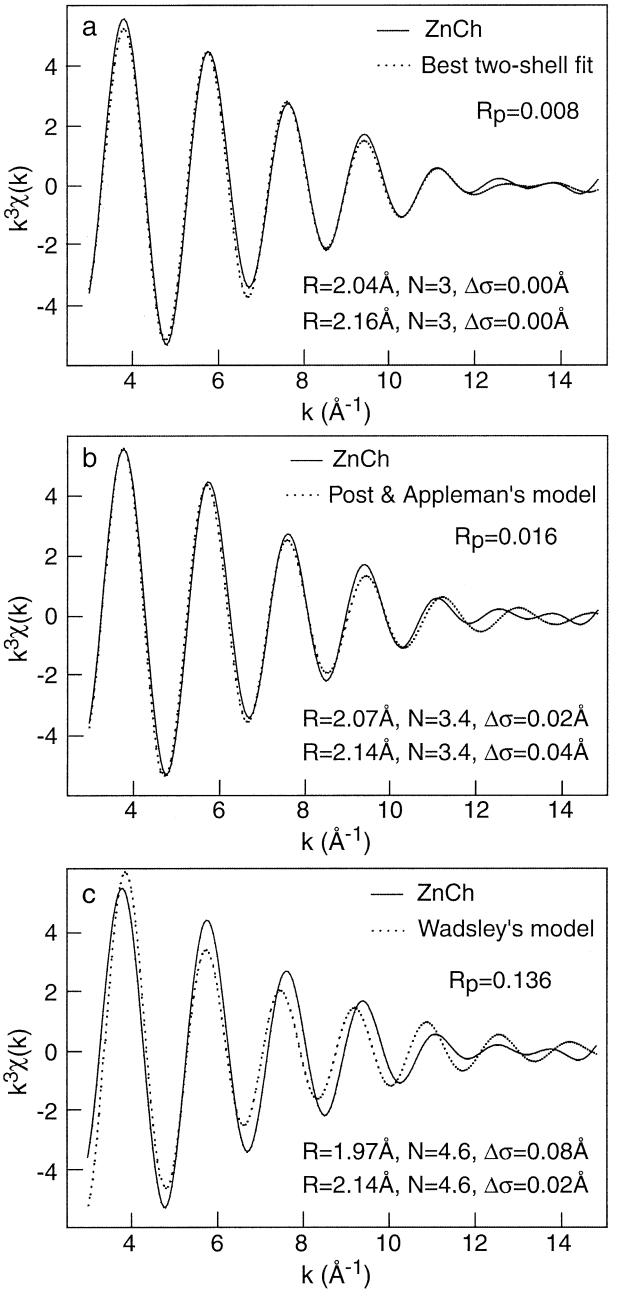

Fig. 7. (a) Best two-shell spectral fit of $k^3\chi_{\text{Zn-O1}}$ for chalcophanite. Comparison of the experimental $k^3\chi_{\text{Zn-O}}$ function for chalcophanite to those calculated from the crystallographic structural models of (b) Post and Appleman (1988) and (c) Wadsley (1955).

is typically 1.96 to 1.98 Å and individual $^{[IV]}$Zn-O distances are generally more coherent than $^{[VI]}$Zn-O distances (Sarret et al., 1998). Therefore, at least three distinct oxygen subshells are likely present in sorption samples, but they cannot be distinguished because the resolution in distance, given by the 3- to 13-$Å^{-1}$ interval fit, is typically 0.1 Å. Consequently, a two-shell model was attempted and proved to be sufficient to correctly simulate all experimental $k^3\chi_{\text{Zn-O1}}$ functions. Values of d(Zn-$O1_1$) are shorter in birnessite than in chalcophanite and decrease from 2.01–2.02 Å to 1.97 Å with increasing Zn concentration, whereas d(Zn-$O1_2$) remains constant at 2.14 to 2.15 Å (Table 2). Clearly, the Zn-$O1_1$ distance is a weighted value between d($^{[VI]}$Zn-$O1_1$) and d($^{[IV]}$Zn-O1), and its decrease reflects the change in relative proportions of the two complexes with increased surface loading.

The nearest Mn shell EXAFS contributions were analyzed by Fourier backtransforming the second RSF peaks in the [2.5 to 3.7] Å $R + \Delta R$ range (Figs. 8a,b). As for χ_{O1} contributions, χ_{Mn1} contributions of ZnBi 8 and ZnBi 69 are shifted to the right indicating a shortening of the average Zn-Mn1 distance. The χ_{Mn1} function of ZnBi 8 displays a marked node pattern at 10.5 $Å^{-1}$, which was satisfactorily reproduced ($R_p = 17 \times 10^{-3}$) by assuming 2.9 Mn at 3.35 Å ($\Delta\sigma = 0.00$ Å) and 2.0 Mn at 3.50 Å ($\Delta\sigma = 0.00$ Å) (Fig. 8c). The longer distance is similar to d($^{[VI]}$Zn-Mn1) in chalcophanite (Table 1) and therefore can be assigned to $^{[VI]}$Zn (complex 2) in the TC position.

Table 2. EXAFS parameters for Zn-O pairs[a].

Sample	Shell	R (Å)	N_O	$\Delta\sigma$ (Å)	R_p
Chalcophanite	2	2.04	3.0	0.00	0.008
		2.16	3.0[b]	0.00	
ZnBi 128	2	2.02	2.6	0.01	0.004
		2.15	2.6[b]	0.01	
ZnBi 69	2	2.01	2.4	0.00	0.003
		2.15	2.4[b]	0.01	
ZnBi 8	1	1.97	3.3	0.02	0.010
	2	1.97	3.8	0.02	0.008
		2.20	0.9	0.02	

[a] Fits performed on $k^3\chi$ using experimental amplitude and phase shift functions extracted from ZnO; the threshold energy ΔE was fixed to 0.0 eV relative to ZnO. Shell = number of fitting shells. $\Delta\sigma$ is the differential Debye-Waller factor relative to ZnO, in ZnO σ = 0.07 Å; R_p is the figure of merit of the spectral fit. N_{Free} = 7 to 8. For one-shell fits, N_{Float} = 3, and for two-shell fits, N_{Float} = 5 to 6.
[b] Value fixed identical to the first subshell.

The shorter d([IV]Zn-Mn1) distance can be attributed to [IV]Zn (complex 1) also at the TC site because Zn in tetrahedral coordination should be closer to the Mn layer.

The consistency among these two Zn-Mn1 distances, the two short Zn-O1 EXAFS distances (O_{layer}, 2.04 and 1.97 Å), and the XRD structural parameters for HBi reported by Lanson et al. (2000) can be evaluated by simple geometrical considerations (Fig. 9). The separation distance between two O_{layer} atoms in an undistorted birnessite layer is d(O-O) = d(Mn-Mn) = d(Mn-□) = b = 2.846 Å. The elevation of [VI]Zn above the O sheet is then equal to $\sqrt{2.04^2 - (2.846/\sqrt{3})^2}$ = 1.21 Å, and the [VI]Zn-Mn1 distance, calculated from the [VI]Zn elevation, the thickness of the Mn layer (2.0 Å) and the Mn-□ distance, is $\sqrt{(1.21 + 1)^2 + 2.846^2}$ = 3.60 Å (Fig. 9a). For the [IV]Zn species, this calculation yields d([IV]Zn-Mn1) = 3.53 Å (Fig. 9b). The two Zn-Mn1 EXAFS distances, predicted from the current HBi structural model and the Zn-O1 EXAFS distances, are clearly much longer than the experimental values (3.35 for [IV]Zn, and 3.50 Å for [VI]Zn). It was possible to reconcile the

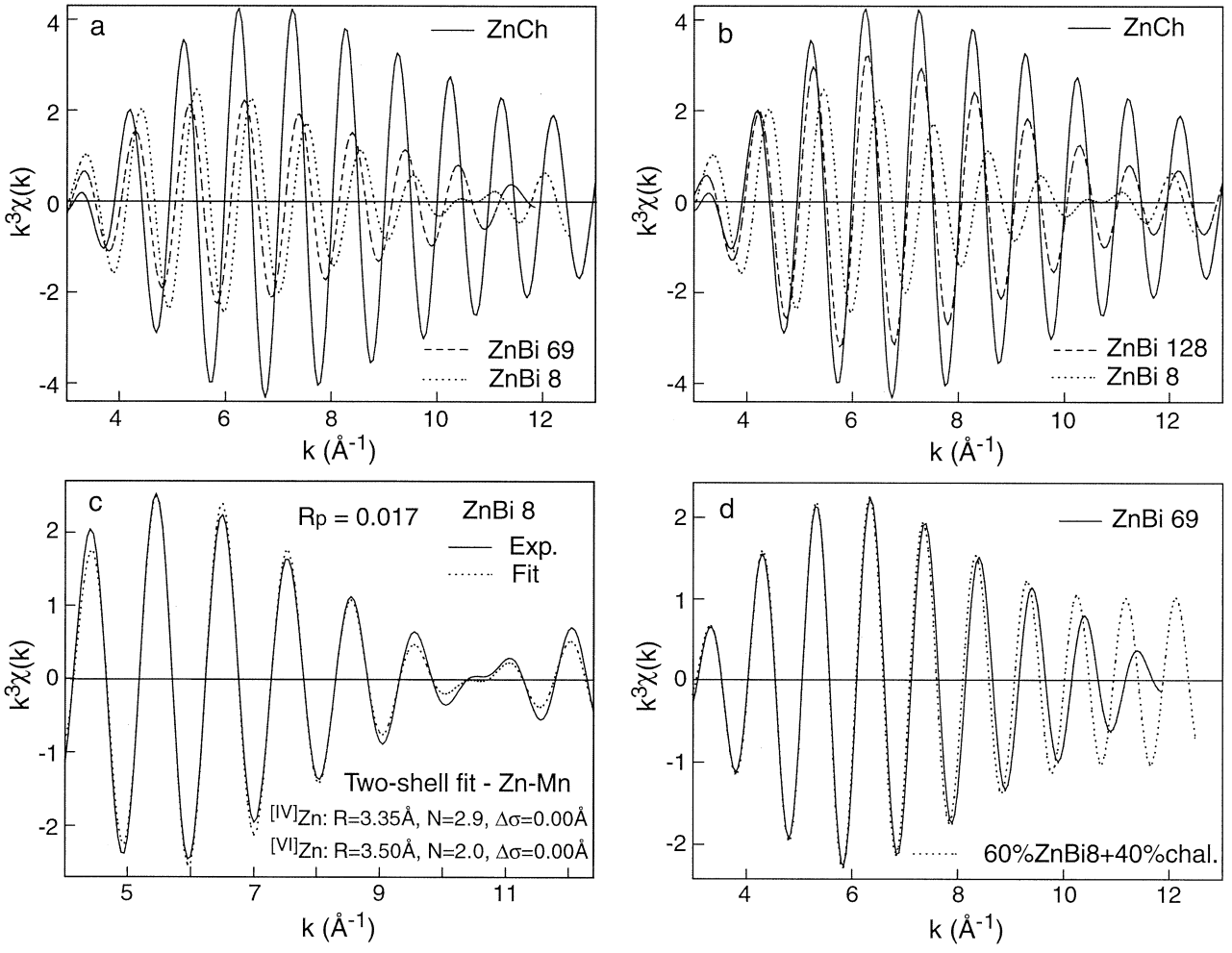

Fig. 8. (a, b) Comparison of $k^3\chi_{Mn1}$ functions for Zn-sorbed birnessite samples and chalcophanite. All birnessite waves are damped because of the structural disorder resulting from the presence of two interlayer complexes ([VI]Zn and [IV]Zn). (c) Best two-shell fit for ZnBi 8, which contains the highest amount of [IV]Zn interlayer complex (complex 1). The short Zn-Mn distance at 3.35 Å corresponds to the [IV]Zn interlayer complex and the long distance at 3.50 Å to the [VI]Zn complex (complex 2). (d) $k^3\chi_{Mn1}$ function for ZnBi 69 and a linear combination of 60% ZnBi 8 + 40% ZnCh.

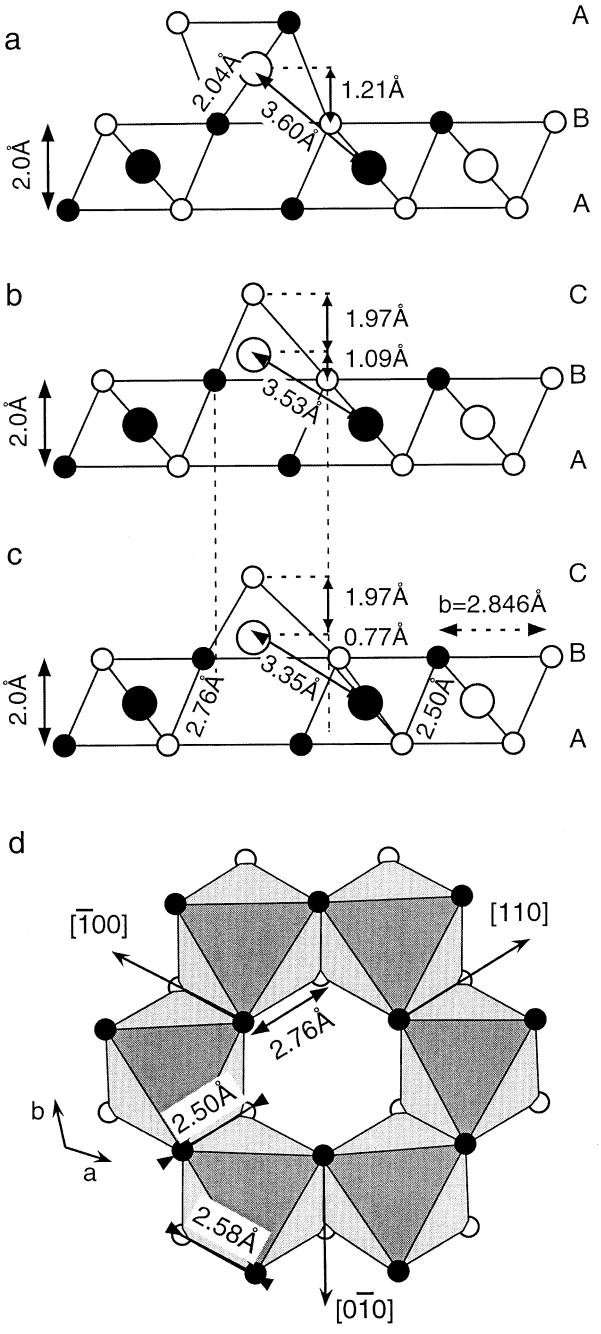

Fig. 9. Structural models for Zn sorbed to octahedral vacancies. In (a) and (b), the filled and empty Mn_{layer} sites have the same size. In this model, two of the four theoretical $^{[VI]}$Zn-O (2.04 Å), $^{[VI]}$Zn-Mn (3.60 Å), $^{[IV]}$Zn-O (1.97 Å), and $^{[IV]}$Zn-Mn (3.53 Å) distances are incompatible with the EXAFS distances (2.04 Å, 3.50 Å, 1.97 Å, and 3.35 Å, respectively). In (c) and (d), the empty Mn_{layer} site is enlarged as a result of the displacement by 0.15 Å in the [110], [$\bar{1}$00], and [0$\bar{1}$0] directions of the six oxygen atoms delimiting the vacancy (three from the upper O sheet and three from the lower O sheet). This deformation, which is common in dioctahedral layer structures, provides good agreement between model and experiment. In (a) to (c), projection is along the b-axis. Open symbols indicate atoms at $y = 0$, and solid symbols indicate atoms at $y = \pm 1/2$. In (d), projection is along the c-axis. Open and solid symbols indicate oxygen atoms of the lower and upper sheet, respectively.

Table 3. EXAFS parameters for Zn-Mn pairs.[a]

Sample	Shell	R (Å)	N_{Mn}	$\Delta\sigma$ (Å)	R_p
ZnBi 128	1	3.48	6.1	0.02	0.008
ZnBi1 69	1	3.45	5.0	0.02	0.019
ZnBi 8	2	3.35	2.9	0.00	0.017
		3.50	2.0	0.00	

[a] Fits performed on $k^3\chi$ using experimental amplitude and phase shift functions extracted from chalcophanite; the threshold energy ΔE was fixed to 0.0 eV relative to chalcophanite. Shell = number of fitting shells. $\Delta\sigma$ is the differential Debye-Waller factor relative to chalcophanite, in chalcophanite $\sigma = 0.09$ Å; R_p is the figure of merit of the spectral fit. $N_{Free} = 7$ to 8. For one-shell fits, $N_{Float} = 3$, and for two-shell fits, $N_{Float} = 6$.

Zn-O1 and Zn-Mn1 EXAFS distances by shifting the O_{layer} atoms of vacant octahedra 0.15 Å in the [110], [$\bar{1}$00] and [0$\bar{1}$0] directions (Figs. 9c,d). This displacement, which is commonly observed in structures of layer silicates and oxides having vacant sites, such as dioctahedral minerals (Hill, 1985), results in an increased length of unshared edges and a decrease of the length of shared edges, thus increasing the size of empty octahedra. For instance, in chalcophanite the length of edges shared with Mn octahedra varies between 2.50 to 2.58 Å, whereas the unshared edges at the border of a vacant site have a length of 2.76 Å (Fig. 9d; Post and Appleman, 1988). This can be understood in terms of the relatively larger electrostatic repulsion between O atoms in the absence of a central cation (unshared edge) and the concomitant improved screening of cationic charges resulting from shortening of the shared edges. Introduction of local distortion of the oxygen sheet yielded d($^{[IV]}$Zn-O1) = 1.95 Å and d($^{[IV]}$Zn-Mn1) = 3.35 Å for the TC $^{[IV]}$Zn complex, and d($^{[VI]}$Zn-$O1_1$) = 2.04 Å and d($^{[VI]}$Zn-Mn1) = 3.49 Å for the TC $^{[VI]}$Zn complex, in good agreement with experimental EXAFS distances for all atomic pairs. This local distortion was undetected by powder XRD (Lanson et al., 2002a), which is insensitive to the difference in size of filled and empty octahedra when they are randomly distributed. In this case, the O-O distance determined by XRD is a weighted average value.

At higher surface coverage, the χ_{Mn1} functions are intermediate between those of ZnCh and ZnBi 8 (Figs. 8a,b). However, linear combinations of these two compounds provided only an approximate fit to experimental functions at high Zn content in contrast to the fit to the χ_{O1} contributions. An example is given by comparing the theoretical 60% ZnBi 8 + 40% ZnCh to the experimental ZnBi 69 waves (Fig. 8d). The two waves are superimposed in the low k range but neither their envelope nor their frequency are coincident above 9 to 10 $Å^{-1}$. A one-shell fit was able to satisfactorily simulate experimental data at intermediate and high Zn content over the entire k range. Best fit Zn-Mn1 distances vary from 3.45 Å (ZnBi 69) to 3.48 Å (ZnBi 128), and are shorter in ZnBi 69 because of the higher proportion of $^{[IV]}$Zn (Table 3). In addition to the reduced Zn-Mn1 distance, the presence of $^{[IV]}$Zn complex in ZnBi 69 and 128 is indicated by the increase of the Debye-Waller disorder term (σ), which is 0.02 Å higher than in the chalcophanite reference. This parameter modifies the damping of the simulated wave. During the least squares fitting of the ZnBi 69 and 128 χ_{Mn1} functions, σ diverged rapidly from its value in

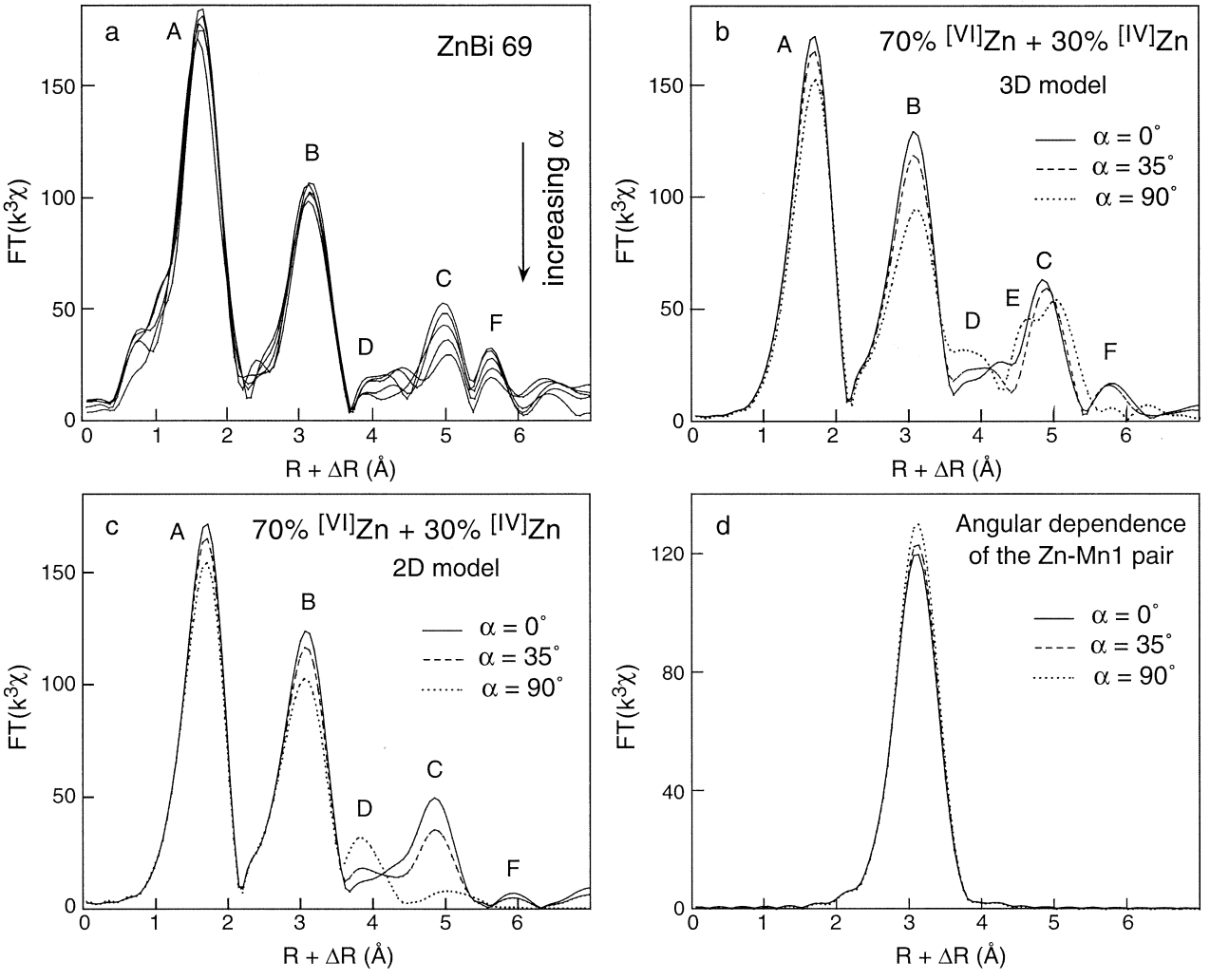

Fig. 10. Experimental (a) and FEFF simulated (b–d) polarized RSFs for ZnBi 69. In (a), the amplitude of RSF peaks gradually decreases with increasing α angle (α = 0°, 20°, 35°, 50°, 90°). Theoretical RSFs were calculated for a 3D (b) and a two-dimensional (2D) (c) cluster made of 70% $^{[VI]}$Zn-containing + 30% $^{[IV]}$Zn-containing chalcophanite particles. Peak B is the sum of the Zn-Mn1 contribution and those from higher distance O shells (3.4 to 3.7 Å). (d) FEFF-simulated Zn-Mn1 contribution. The amplitude of RSF peaks increases with α when the β angle is lower than the magic angle of 54.7°.

ZnCh because the birnessite and chalcophanite waves have similar amplitudes near 4 to 5 Å^{-1} and then increasingly different amplitudes at higher k value (Figs. 8a,c). In these simulations, the larger spread of the Zn-Mn1 distances in sorption samples was modeled by assuming a gaussian distribution of distances ($\Delta\sigma$). For example, the Mn1 shell of ZnBi 69 was fitted with 5.0 Mn at the average distance of 3.45 Å with a continuous distribution in distances of 0.02 Å half-width (R_p = 0.019, Table 3). The precision of N_{Mn1} was estimated by varying σ: $\Delta\sigma$ = 0.03 Å yielded N_{Mn1} = 6.0 and R_p = 0.04, and $\Delta\sigma$ = 0.01 Å yielded N_{Mn1} = 4.2 and R_p = 0.038. When R_p was twice its optimal value, the spectral fit degraded visibly, and it was concluded that the 4.2 to 6.0 interval represents the maximum range for the variation of N_{Mn1} in this sample (~20%). In ZnBi128, N_{Mn1} is close to 6, meaning that the distribution of the Zn-Mn1 distances is narrower in this sample.

In conclusion, quantitative analysis of Zn-O1 and Zn-Mn1 EXAFS contributions shows that solution Zn sorbs above vacant layer sites as a tetrahedrally coordinated interlayer complex at low concentration, and preferentially as a chalcophanite-like octahedral complex at higher surface loading. The distribution of interatomic distances resulting from the mixing of $^{[IV]}$Zn and $^{[VI]}$Zn surface species accounts, at least partly, for the marked decrease in amplitude, and shift in frequency and distance, of EXAFS spectra and RSFs for Zn-sorbed birnessite compared with chalcophanite. As will be shown below, polarized EXAFS spectroscopy provides further insight on the local environments of Zn in these two phyllomanganates.

4.1.2. Polarized EXAFS

Peaks C and F in the polarized-RSF (P-RSF) of ZnBi 69 are angularly dependent on polarization, whereas peaks A and B are not (Fig. 10a). The variation in amplitude of peaks C and F undoubtedly has a structural origin for several reasons. First, P-EXAFS spectra of ZnBi 69 have the same signal to noise

ratio for all experimental angles (data not shown) and, consequently, the same is true for P-RSFs. Second, if higher distance RSF peaks were a result of noise, their variation in amplitude would not have a regular α dependence as observed experimentally. Third, the bigger amplitude reduction for peaks C and F than for A and B cannot be due to poorer S/N ratio because noise is intrinsically constant over the whole $R + \Delta R$ range.

Experimental P-RSFs were interpreted by calculating *ab initio* P-RSFs for an ideally textured film composed of 70% $^{[VI]}$Zn-containing and 30% $^{[IV]}$Zn-containing chalcophanite particles based on the fraction of complex 1 in ZnBi 69 determined by powder EXAFS spectroscopy. The $^{[IV]}$Zn-containing chalcophanite model was built by replacing the $^{[VI]}Zn(O,H_2O)_6$ interlayer complex in ZnCh by a $^{[IV]}ZnO_4$ complex (d($^{[IV]}$Zn-O_{layer}) = 1.97 Å, d($^{[IV]}$Zn-Mn1) = 3.35 Å, d($^{[IV]}$Zn-□-$^{[IV]}$Zn) = 3.54 Å). All single (SS, χ_2) and multiple (MS, χ_{3-4}) scattering path contributions of successive atomic shells were computed for distances up to 8.4 Å from the central Zn atom for a 3D periodic theoretical crystal and also for a one layer (2D) crystal. The cutoff in magnitude of paths was set to 5% of the mean amplitude of the first coordination shell, and the many-body reduction factor S_0^2 was fixed to 0.85 for all spectra (O'Day et al., 1994; Manceau et al., 1998). The σ values were taken to be 0.08 Å for Zn-O1, 0.09 Å for Zn-Mn1, 0.1 Å for SS paths of other shells, and 0.11 Å for all MS paths for the 3D model based on previous values determined on CoOOH and Garfield nontronite (Manceau et al., 1998, 1999a). In the 2D model, σ values were taken to be 0.08 Å, 0.09 Å, 0.12 Å, and 0.12 Å, respectively, to account for the higher structural disorder of birnessite than chalcophanite layers. Theoretical P-RSFs at $\alpha = 0°$, 35°, and 90° for the 3D and the 2D models are presented in Figures 10b and 10c, respectively. The exact nature of each peak was determined by examining the intensities of SS and MS paths, and the angular dependence of each peak was interpreted from the crystallographic orientation of atomic pairs in the corresponding atomic shell (β angle in Table 1). For SS paths, the weight of a given shell, represented by its effective number (N_{polar}) of atoms, is (Manceau et al., 1998)

$$N_{polar} = 3N_{powder}[\cos^2\beta \sin^2\alpha + (\sin^2\beta\cos^2\alpha)/2], \quad (2)$$

where N_{powder} represents the crystallographic number of atoms in the shell, and β is the angle between the atomic pair and the layer normal. In the parallel ($\alpha = 0°$) and normal ($\alpha = 90°$) orientations of the electric field vector, Eqn. 2 reduces to

$$N^{\parallel}_{polar} = \frac{3}{2} N_{cryst} \sin^2\beta \quad (3)$$

$$N^{\parallel}_{polar} = 3N_{cryst} \cos^2\beta. \quad (4)$$

From Eqn. 2, when $\beta = 54.7°$, $N_{polar} = N_{cryst}$, which means that the atomic pair has no polarization dependence in the X-ray beam. Its contribution to EXAFS is thus constant and equal to that in a powder regardless of α. For $\beta < 54.7°$, $\chi(k,\alpha)$ increases with α, whereas for $\beta > 54.7°$, $\chi(k,\alpha)$ decreases with increasing α. The main conclusions of this analysis are summarized below.

(1) Peak A originates from the O1 shell. Its amplitude decreases when α increases as expected from the angular variation of N_{polar} for the two types of complexes ($N^{\parallel}_{O1}$ = 6.1 and $N^{\perp}_{O1}$ = 5.7 for $^{[VI]}$Zn and $N^{\parallel}_{O1}$ = 4.5 and $N^{\perp}_{O1}$ = 3.8 for $^{[IV]}$Zn, Table 1).

(2) Peak B corresponds to the overlapping contribution of the nearest Mn1 shell and O shells at 3.4 to 3.7 Å (Table 1). The SS contribution of the Zn-Mn1 shell predominates and has an amplitude that increases slightly with α because the predominant $^{[VI]}$Zn-Mn1 pair has a β angle of 53.6°, and the less abundant $^{[IV]}$Zn-Mn1 pair a β angle of 56.4° (Fig. 10d). When the O shells are added to the calculations, peak B has a reverse α dependence (Figs. 10b,c). The decrease in peak B with α in the 3D model is relatively greater because of the strong anisotropic contribution of oxygen atoms from adjacent layers for $^{[VI]}$Zn: $N^{\parallel}_{O1}$ = 3.8 and $N^{\perp}_{O1}$ = 1.4 (Table 1).

(3) Peak D originates from the Zn1 shell located on either side of the layer Mn vacant site (Fig. 2). This peak has zero intensity in the parallel orientation and is greatly amplified in the perpendicular orientation because $\beta_{Zn\text{-}Zn1} = 0°$. It has a pure SS origin owing to the absence of Mn layer atoms collinear to the Zn-Zn1 pair.

(4) Peak E results from the SS contributions of the three $Mn1_{adj}$ atoms (R = 5.14 Å) from adjacent layers and is only observed at $\alpha = 90°$ ($\beta = 19°$) in the 3D model. Chalcophanite has a three-layer periodicity ($\bar{3}R$ space group) and the mutual arrangement of successive layers can be described by the usual close-packed notation A, B, and C, and a, b, c; capital letters stand for unequivalent crystallographic O and H_2O sites, and lowercase letters stand for the positions of Mn and Zn. In this symbolic representation, the three-layer stack can be denoted . . . AcBc'A'b'CbAb'C'a'BaC . . . , where prime notation stands for interlayer Zn and H_2O positions. Anions from successive sheets are close packed (ABA'CAC'BC); therefore, O_{adj} shells always contain three atoms (Table 1). Likewise, Zn atoms are always surrounded by three cations from adjacent sheets (c'b', c'b, b'a', b'a stack . . .). The fact that P-EXAFS spectroscopy is sensitive to the stacking mode of layered structures (see also Manceau et al., 1999a,b) will be used below to interpret ZnBi 69 P-RSFs.

(5) Peaks C and F arise from SS and MS scattering paths with the second and third next nearest Mn layer shells (Mn2 and Mn3, Table 1).

The theoretical explanations of P-RSF peaks will now be applied to ZnBi 69. The weak, but significant, lowering of peak A with increasing α (Fig. 10a) indicates that the Zn-O1 pair has an average β angle slightly lower than 57.4°. Its smaller angular dependence compared with theory likely originates from an imperfect alignment of birnessite platelets in the film plane (Manceau and Schlegel, 2001). Peak B of ZnBi 69 has a markedly lower angular variation than predicted from theory, and this is even more true for the 3D model. FEFF calculations showed that this multishell peak contains contributions from the layer Mn1, O2, and O3 shells, and from the O_{adj} shell, and that O shells are more dichroic than the Mn1 shell. The reduction of the experimental angular dependence is clearly too high to stem uniquely from a texture effect, and it likely partly originates from a difference of structure between birnessite and chalcophanite. In chalcophanite, the three oxygen atoms in

each of the three higher O shells (O2, O3, and $O1_{adj}$) are located at the same distance from Zn as a result of the hexagonal symmetry of chalcophanite layers ($a = b\sqrt{3}$) and the displacement of adjacent layers along [110] by $(\vec{a} - \vec{b})/3$. In contrast to chalcophanite, which contains only tetravalent Mn atoms, ZnBi 69 contains ~13% of Mn^{3+} in its octahedral layer, and this Jahn-Teller cation lowers the symmetry of the oxygen framework. Therefore, Zn-O layer distances and β angles should be less coherent in birnessite than in chalcophanite. The $Zn\text{-}O_{adj}$ distances should be also less coherent in Zn-sorbed birnessite because, although adjacent Mn layers are translated by $+a/3$ as in chalcophanite, monoclinic ZnBi crystallites contain typically 12 to 15% hexagonal and random stacking faults (Lanson et al., 2002a). As explained previously, simulation of the larger disorder of birnessite particles was achieved by increasing the σ value of SS paths for higher shells and of MS paths in the FEFF simulation for the 2D model (Fig. 10c). Comparison of peak B in Figures 10a and 10c shows that the agreement between theory and experiment is incomplete. The difference can be attributed partly to an imperfect film texture.

Another difference between ZnBi 69 and calculated P-RSFs is the absence, or weak intensity, of peak D at $\alpha = 90°$ in birnessite. FEFF simulations showed that this peak originates in chalcophanite from Zn-Zn pairs across $\square_{Mn}$. Its low intensity is in apparent contradiction with the presence of chalcophanite crystallites identified by SAED (Drits et al., 2002) and of TC-pairs above Mn vacant sites identified by XRD (Lanson et al., 2002a). At least six local configurations may be encountered: $^{[VI]}Zn\text{-}\square\text{-}^{[VI]}Zn$, $^{[IV]}Zn\text{-}\square\text{-}^{[VI]}Zn$, $^{[IV]}Zn\text{-}\square\text{-}^{[IV]}Zn$, $^{[VI]}Zn\text{-}\square\text{-}Mn^{3+}$, $^{[IV]}Zn\text{-}\square\text{-}Mn^{3+}$, and $^{[IV]}Zn\text{-}\square\text{-}\square$, with each Zn-Me pair having a specific bond length. Hence, the structural disorder arising from this multiplicity of local structures can explain the weakening of peak D in ZnBi 69 relative to chalcophanite.

The angular dependence of peak C (Mn2 shell) for ZnBi 69 is intermediate between those calculated for the 3D and 2D chalcophanite models, but the striking difference is the absence at $\alpha = 90°$ in the experimental spectrum of shoulder E in the 3D model. In chalcophanite this peak originates from $Mn1_{adj}$ interactions (Fig. 2), and its absence can be explained by several reasons. In ZnBi 69 the $Me1_{adj}$ contribution is shifted to a higher distance and adds to the Mn2 contribution (peak C) because birnessite has a larger interlayer spacing (7.06 Å) than chalcophanite (6.93 Å). Another reason is the incoherence of the $Zn\text{-}Me1_{adj}$ distances in birnessite resulting from the varieties of coordination geometries (e.g., [VI] vs. [IV]) and combinations of paired atoms in birnessite compared with chalcophanite, as described previously for TC-pairs. A third source of disorder is the presence of stacking faults, which modify Zn-Me distances between two faulted oxygen planes.

In conclusion, the quantitative analysis of polarized EXAFS data for ZnBi 69 sheds direct light on the in-plane and out-of-plane local environment of Zn sorbed on birnessite. The results provide firm evidence for the sorption of Zn above $\square_{Mn}$ as in chalcophanite, but sorbed Zn has a more disordered short to midrange structure than in the stoichiometric phyllomanganate reference. The structural disorder about Zn atoms comes from chemical, crystallographic and physical heterogeneities. These include a mixing of Mn oxidation states in the layer and interlayer of the sorbent, the presence of two Zn interlayer complexes having a different coordination number, and the disruption of the 3D monoclinic periodicity caused by the presence of hexagonally packed oxygen sheets.

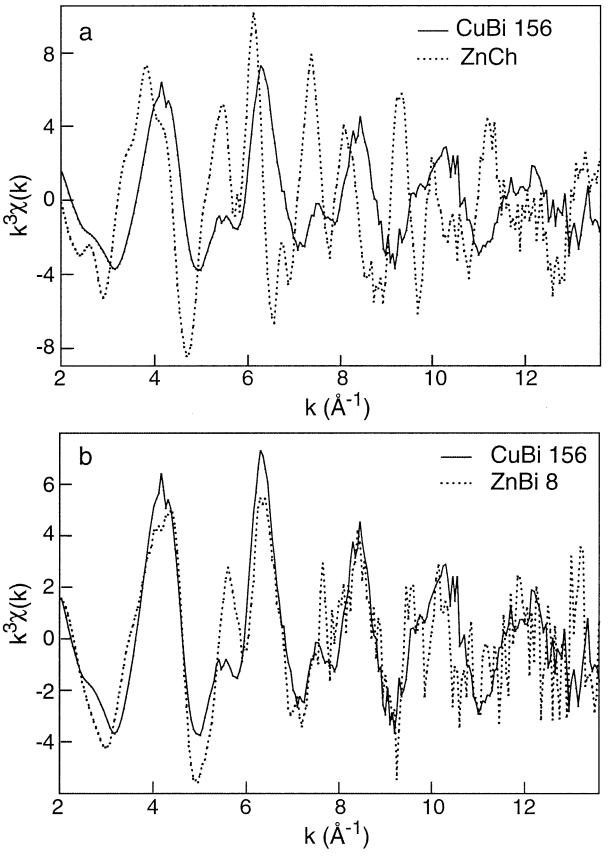

Fig. 11. Comparison of Zn and Cu K-edge k^3-weighted EXAFS spectra for chalcophanite and CuBi 156 (a) and for ZnBi 8 and CuBi 156 (b). The wave frequency of CuBi 156 is shifted to high k values relative to chalcophanite and almost superimposed on that of ZnBi 8. This observation indicates that Cu occupies the same crystallographic site (TC complex) and has similar interatomic distances as Zn in ZnBi 8.

4.2. Cu K-Edge

The Cu K-edge EXAFS spectrum and RSF of CuBi 156 are compared with Zn K-edge data for ZnCh and ZnBi 8 in Figures 11 and 12. The entire EXAFS signal of CuBi 156 is shifted to high wave-vector values compared with chalcophanite but is almost superimposed on ZnBi 8, which suggests that Cu in CuBi 156 and Zn in ZnBi 8 have similar interatomic distances. This inference is confirmed by the comparison of RSFs (Fig. 12), which in addition indicates that the similarity in distance between these two samples extends to ~5.5 Å, although d(Cu-Mn1) is clearly larger than d(Zn-Mn1) (peak B).

A one-shell least squares fit of $\chi_{Cu\text{-}O1}$ yielded approximately 4 O at 1.96 Å ($\Delta\sigma = 0.00$ Å, $\Delta E = 0.0$ eV, $R_p = 0.012$; Fig. 13a). This distance is typical of the equatorial Cu^{2+}-O distance in a Jahn-Teller distorted CuO_6 octahedron (Douglas et al., 1994). Close examination of Fig. 13a reveals that the wave phase was precisely reproduced for $k > 9$ Å^{-1} but not below.

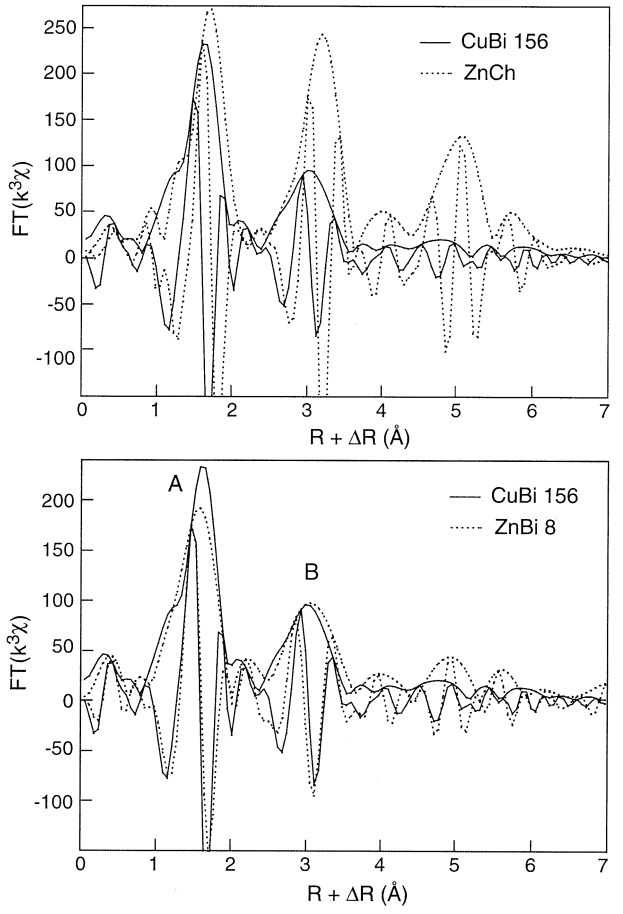

Fig. 12. Zn and Cu K-edge RSFs derived from the EXAFS spectra presented in Fig. 11. In CuBi 156, interatomic distances are shorter than in chalcophanite and similar to those in ZnBi 8, in agreement with the difference in wave frequencies observed in EXAFS spectra (Fig. 11).

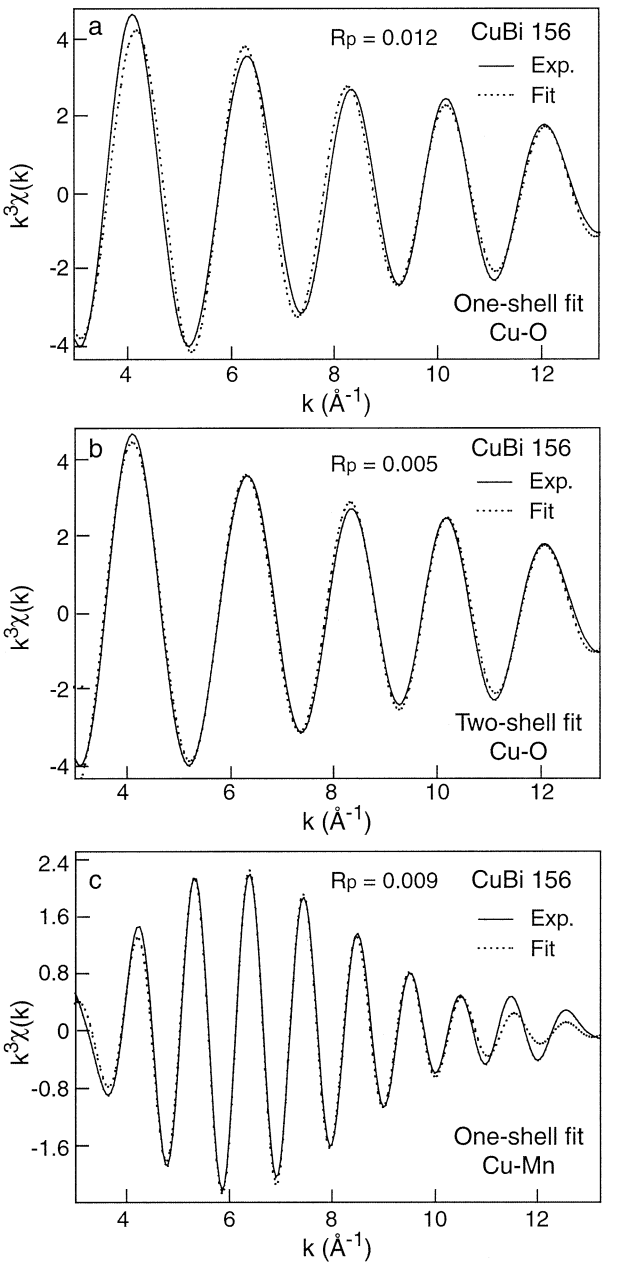

Fig. 13. Fourier-filtered $\chi_{\text{Cu-O1}}$ (a, b) and $\chi_{\text{Cu-Mn1}}$ (c) contributions to EXAFS spectra (solid lines) with fits (dotted lines) for CuBi 156.

The theoretical curve is shifted to the right in the 3–5 $Å^{-1}$ interval and to the left in the 6.5- to 9-$Å^{-1}$ interval. In addition, the amplitude of the theoretical spectrum is slightly too low for $k < 5$ $Å^{-1}$ and 10 $Å^{-1} < k < 11$ $Å^{-1}$, and slightly too high for 5 $Å^{-1} < k < 8.5$ $Å^{-1}$. These phase and amplitude mismatches suggest the presence of a weak second wave that interferes destructively at $k \sim 6$ $Å^{-1}$, which would correspond to a second oxygen shell separated from that at 1.96 Å by $\Delta R \sim \pi/(2 \times 6\ Å^{-1}) \sim 0.26$ Å. Because in a Jahn-Teller environment Cu^{2+} completes its octahedral coordination by two axial oxygen atoms at 2.2 to 2.3 Å, a two-shell fit was attempted. Better agreement between experiment and theory was obtained by assuming four O at 1.96 Å ($\Delta\sigma = 0.01$ Å) and two O at 2.23 Å ($\Delta\sigma = 0.01$ Å, $\Delta E = 0.0$ eV, $R_p = 0.005$, Fig. 13b). This interpretation is structurally and physically preferable to the one-shell model. The first shell of Mn atoms (peak B in Fig. 12b) was best modeled with 5.4 Mn at 3.43 Å ($\Delta\sigma = 0.03$ Å, $\Delta E = 1.1$ eV, Fig. 13c).

This analysis indicates that Cu^{2+} forms a $^{[VI]}$TC interlayer complex above $\square_{Mn}$ like Zn at high surface loading. The 0.03 Å increase in the differential disorder term ($\Delta\sigma$), and the decrease of N_{Mn} from ideally 6.0 to 5.4, relative to chalcophanite, are significant. The opposite variations of $\Delta\sigma$ and N indicate a greater spread in the average Cu-Mn bond distance in birnessite. As for Zn, the distribution of Cu-Mn distances around $<R> = 3.43$ Å can be attributed to the presence of Mn^{3+} and Mn^{4+} cations in the manganese layer but, unlike Zn, an additional disorder component comes from the Jahn-Teller distortion of the Cu octahedron. Interestingly, despite the fact that Cu is sixfold coordinated and occupies the same surface site in birnessite as $^{[VI]}$Zn in chalcophanite, its EXAFS spectrum is much different from that of chalcophanite, and is

fortuitously similar to that of ZnBi 8, which has $^{[VI]}$Zn and $^{[IV]}$Zn TC interlayer complexes (Fig. 11). This peculiarity stems from the d^9 electronic structure of Cu^{2+}, which results in four short $^{[VI]}$Cu-O distances (1.96 Å) that are almost identical to d($^{[IV]}$Zn-O) (1.97 Å), and two long $^{[VI]}$Cu-O distances (~2.2 −2.3 Å) that are similar to d($^{[VI]}$Zn-H_2O) (~2.14 to 2.20 Å). Because the three atoms delimiting the octahedral hole correspond to oxygen and the interlayer ligands are water molecules, for geometrical reasons the equatorial plane of the Cu^{2+} octahedron should consist of two O_{layer} and two H_2O, and the two perpendicular axial ligands of one O_{layer} and one H_2O. This particular symmetry of the sorbed species contrasts with that of Zn in chalcophanite and birnessite in which the three Zn-O_{layer} bonds are the shortest, and the three Zn-H_2O bonds the longest.

4.3. Pb L_3-Edge

The stereochemistry of Pb^{2+} is quite complicated as a result of its $6s^2$ outer shell electronic configuration, these two lone pair electrons causing a strong distortion of Pb^{2+} polyhedra (Galy et al., 1975; Manceau et al., 1996; Bargar, 1997a; Sarret et al., 1998). Another source of complexity for the structural study of Pb^{2+} comes from the high variability of its coordination number. Practically all possible coordination numbers between 3 and 12 have been described in the literature (Sahl, 1974), and in some compounds Pb^{2+} coordination numbers are so high that the limit of the lead coordination shell is difficult to assess precisely making the geometry of polyhedra ill-defined. This has been exemplified in the introduction with quenselite in which lead is surrounded successively by four nearest oxygen atoms at 2.22 to 2.76 Å, two next-nearest at 2.99 and 3.16 Å, and two more distant at 4.38 and 4.99 Å, completing a highly distorted cubic coordination. In these conditions, the standard EXAFS equation, which assumes a gaussian distribution of atoms about the absorbing atom, fails at determining the full distribution of interatomic distances present in the different coordination shells. The error in coordination numbers may be quite high and is difficult to assess precisely because in the case of severely distorted coordination shells, the obtained *N* values refer to the closest atoms in the shell. In highly disordered systems, *N* can be too small by a factor of two (Crozier et al., 1988). For this element, therefore, emphasis will not be placed on *N* values when interpreting the data. From an experimental point of view, structural disorder severely decreases the amplitude of the EXAFS signal. This effect is illustrated in Figure 14a, in which $k^3\chi$ spectra for ZnBi 128 and PbBi 31 are compared. EXAFS oscillations are typically five times less intense at the Pb L_3- than the Zn K-edge making it difficult to obtain high signal to noise ratio spectra above ~7 $Å^{-1}$. For this reason extreme care is needed to record high quality lead EXAFS spectra, and these experimental difficulties partly explain the relative paucity of EXAFS studies performed on this environmentally important element (Manceau et al., 1996; Bargar et al., 1997a,b; Morin et al., 1999; Ostergren et al., 1999; Matocha et al., 2001).

In disordered systems, the motion of atoms may also be anharmonic and the incorrect assumption of a gaussian distribution yields interatomic distances that are too small. For instance, the apparent contraction of the Pb-O distance reached ~0.2 Å in $PbSiO_3$ (Manceau et al., 1996). The anharmonicity of the vibration is diminished at temperatures lower than the Einstein or Debye characteristic temperature of the considered compound. This temperature is unknown in Pb sorption samples, but it may be low as in elemental lead (105K) or $PbSiO_3$. To test the possible influence of this effect, the X-ray absorption spectrum of PbBi 31 was recorded at room temperature (PbBi 31RT) and 10 K (PbBi 31He). Figures 14b and 15a show that the signal is globally amplified at 10 K as a result of the freezing of atoms in the structure, and this is especially true at $k > 6$ $Å^{-1}$. This modification of the spectral shape is associated with a shift of neither the wave frequency in reciprocal space (Fig. 14b), nor the imaginary part of the FT (Fig. 15a). This result contrasts strongly with that obtained for $PbSiO_3$, which had its first RSF peak shifted to higher distance at low temperature (Fig. 2 in Manceau et al., 1996). The independence on temperature of the Pb-O (peak A in Fig. 15a) and Pb-second shell (peak B in Fig. 15a) distances in birnessite indicates that EXAFS distances obtained at room temperature by assuming a gaussian distribution are reliable. Therefore, the structural disorder observed in birnessite EXAFS spectra has a static origin.

Figures 14 and 15 show that birnessites have very similar EXAFS signals and RSFs over the entire concentration range investigated ($0.001 \leq Pb/Mn \leq 0.058$), which suggests that the sorption mechanism of Pb is almost independent of the surface loading. For all samples, χ_O partial EXAFS contributions were first fitted to the EXAFS equation by using a single oxygen shell and theoretical standards calculated by FEFF 7. The correctness of theoretical backscattering amplitude and phase shift functions was tested on αPbO and βPbO_2 (Table 4). EXAFS and crystallographic distances were found to coincide to within 0.01 Å in these two references. The main frequency of χ_O for birnessites was broadly reproduced with about one to two oxygen atoms at 2.31 to 2.37 Å (Figs. 16a,b). Similar distance ranges were reported for Pb^{2+} sorption complexes on Fe, Al, and Mn oxides (Manceau et al., 1992, 1996; Bargar et al., 1997a,b; Matocha et al., 2001). However, this one-shell model did not correctly match the experimental signal in any of the birnessite samples; experimental and theoretical waves were clearly shifted at low and high *k* values. The goodness-of-fit parameter was approximately halved by assuming two discrete oxygen subshells at 2.3 Å and ~2.4 to 2.5 Å (Table 4; Figs. 16c,d). This structural model provided a better match to the experimental data and, specifically, to the experimental phase, but the agreement remained unsatisfying. As discussed previously, oxygen atoms are located at varying distances from Pb, and the assumption of two discrete subshells is inadequate to reproduce the large spread of higher Pb-O distances. It has been suggested that Pb^{2+} was oxidized to Pb^{4+} in contact with manganates (Goldberg, 1965; Gadde and Laitinen, 1974; Hem, 1978; Dillard et al., 1981, 1982), but this hypothesis is not supported by our nor other (Matocha et al., 2001) EXAFS results because Pb^{4+}-O distances are systematically shorter than 2.20 Å (Manceau et al., 1996) (e.g., d(Pb^{4+}-O) = 2.16 Å in PbO_2; d'Antonio and Santoro, 1980).

Second RSF peaks systematically possess a shoulder on their right tail (see arrows in Fig. 15), indicating the presence of two cationic shells (Me1 and Me2). This feature was also present in the RSF of Pb-sorbed birnessite reported by Matocha et al. (Fig. 5 in Matocha et al., 2001), but they used only a one cation shell fit. Partial EXAFS spectra obtained by Fourier backtrans-

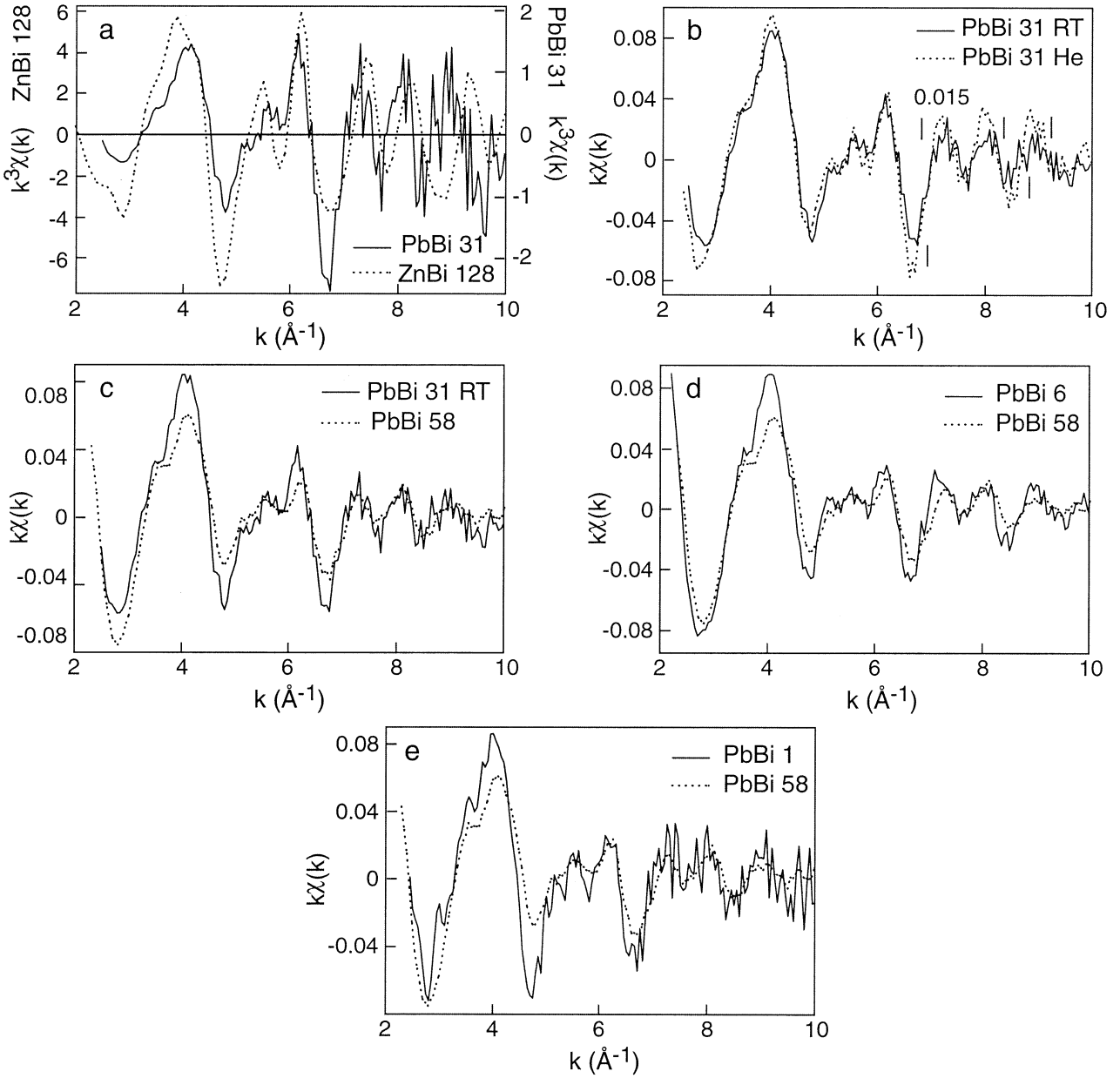

Fig. 14. (a) Comparison of k^3-weighted Zn K-edge and Pb L_3-edge EXAFS spectra for ZnBi 128 and PbBi 31, respectively. (b–e) k-weighted L_3-edge EXAFS spectra for sorption samples.

forming second RSF peaks ($k\chi_{2\text{ndpeak}}$) in the [2.5 to 4.6] Å $R + \Delta R$ range are presented in Fig. 17. All electronic waves are in phase in the whole reciprocal range as expected from the superposition of the imaginary parts in the real space (Fig. 15). Second atomic shells are thus presumably constituted by the same type of atoms at similar average distances from Pb. The nature of atoms in the Me1 shell was identified by excluding the Me2 contribution at about $R + \Delta R = 4.1$ Å from the FT^{-1} of PbBi 6 (arrow in Fig. 15c). The χ_{Me1} wave function thereby obtained by selecting the [2.5 to 3.9] Å $R + \Delta R$ FT^{-1} interval differed significantly from that obtained with the extended [2.5 to 4.6] Å $R + \Delta R$ interval (Fig. 17c): it has a maximum at [5 to 6] $Å^{-1}$, which is characteristic of a single transition metal shell contribution (Teo, 1986). In keeping with this observation, the assumption of a unique Mn shell at 3.77 Å yielded an optimal fit to all sorption samples (Fig. 18a). This distance is close to the 3.74-Å value obtained by Matocha et al. (2001). The assumption of a Pb-Pb, instead of a Pb-Mn, pair resulted in a poor spectral fit because these two atomic pairs have contrasting scattering functions (Fig. 18b). The Pb-Pb amplitude and phase shift functions have a minimum in the [5.7 to 7] $Å^{-1}$ interval (Teo, 1986) that yields a characteristic beat node pattern in the electronic wave (see arrow in Fig. 18b). This distinctive feature allows us to conclude that the first cationic subshell of Pb in birnessite is made of Mn atoms. The increase of the Pb-Mn distance (3.77 Å) compared with Zn-Mn in

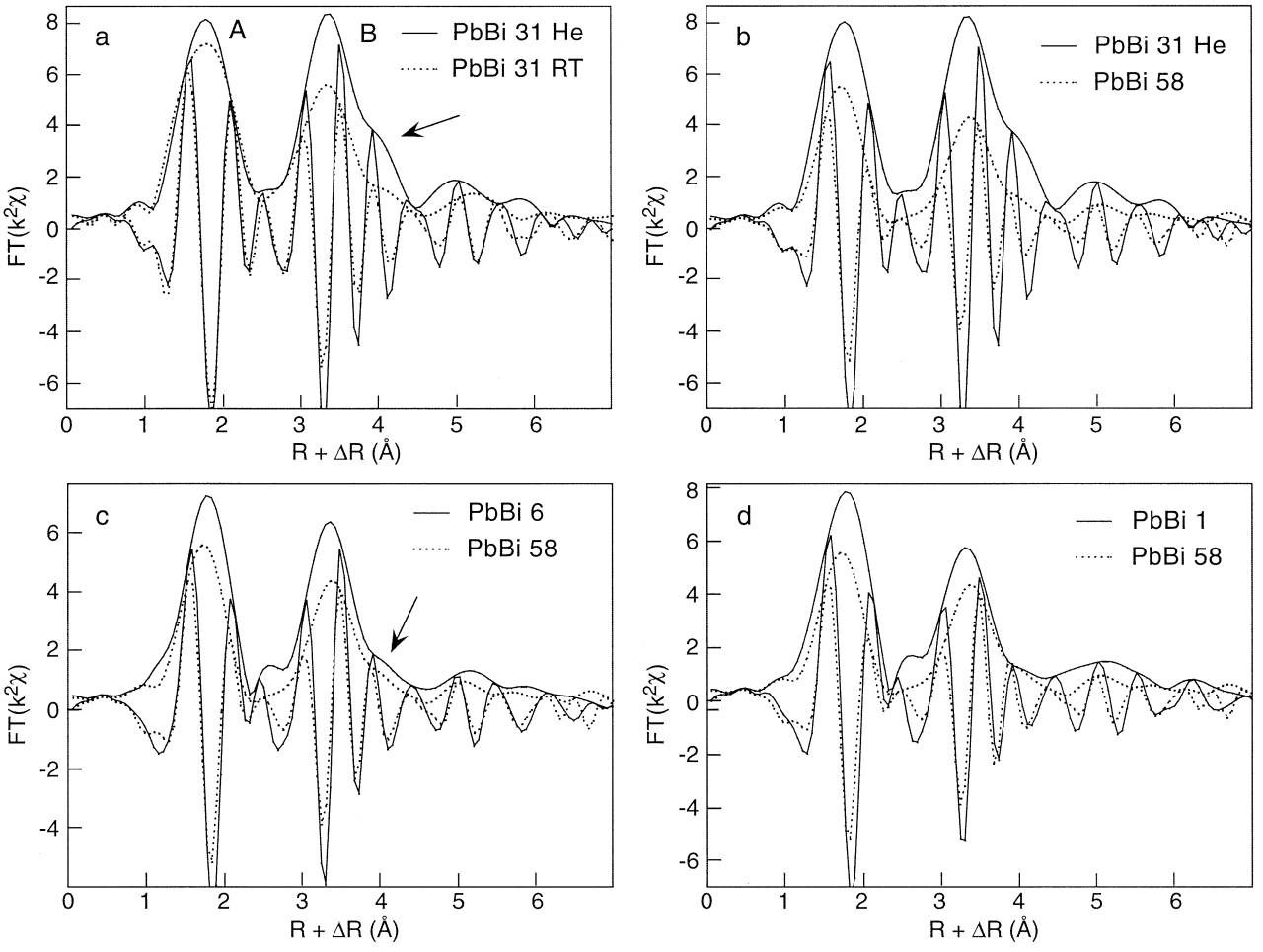

Fig. 15. k^2-weighted Fourier transforms of EXAFS spectra for PbBi samples.

chalcophanite (3.50 Å) matches reasonably well the difference in ionic radii between Pb^{2+} (pyramidal and six-fold coordination) and $^{[VI]}Zn^{2+}$ (0.94 to 1.18 Å vs. 0.74 Å; Shannon and Prewitt, 1969), and this agreement supports the conclusion that Pb forms TC interlayer complexes like Zn and Cu.

The $k\chi_{2ndpeak}$ functions obtained over the extended [2.5 to 4.6] Å $R + \Delta R$ interval exhibit a minimum at ~5 $Å^{-1}$ followed by a maximum at 6.5 to 7.0 $Å^{-1}$ (Fig. 17). This valley in the amplitude is deep in PbBi 31 and its $k\chi_{2nd\ peak}$ function was least squares fitted by assuming successively the presence of Mn or Pb in the Me2 shell. The first hypothesis yielded ~1.7 Mn at 3.80 Å and ~1.3 Mn at 4.61 Å (R_p = 0.013,), and the second ~1.6 Mn at 3.78 Å and ~0.7 Pb at 4.61 Å (R_p = 0.013; Table 5; Figs. 18c,d). The two models have the same R_p values and are thus statistically equivalent over the whole k range. However, the assumption of a Pb subshell gave an extra beat node pattern in the [6.5 to 7.5] $Å^{-1}$ interval owing to the distinctive properties of the Pb-Pb scattering function in this region and therefore failed at reproducing the experimental amplitude at 6.5 to 7.0 $Å^{-1}$. The experimental wave envelope, and specifically its minimum at ~5 $Å^{-1}$, were correctly simulated in the [3 to 8.5] $Å^{-1}$ range by the first structural model (k_{beat} = 3π/2(4.61–3.76) = 5.5 $Å^{-1}$). In neither of these two structural models was the [8.5 to 10] $Å^{-1}$ wave vector range

Table 4. EXAFS parameters for Pb-O pairs.[a]

Sample		Shell	R (Å)	N_O	σ (Å)	R_p
αPbO	XRD	1	2.31	4		
	EXAFS	1	2.31	4.0	0.08	0.01
αPbO_2	XRD	1	2.16	6		
	EXAFS	1	2.16	5.2	0.07	0.005
PbBi 58	EXAFS	1	2.31	1.1	0.09	0.09
		2	2.29	1.0	0.09	0.06
			2.41	1.0	0.10	
PbBi 31RT	EXAFS	1	2.35	1.6	0.08	0.10
PbBi 31He	EXAFS	1	2.34	1.6	0.07	0.09
		2	2.36	2.8	0.10	0.05
			2.69	1.8	0.11	
PbBi6	EXAFS	1	2.35	1.4	0.08	0.04
		2	2.32	1.0	0.07	0.03
			2.45	0.09	0.11	
PbBi 1	EXAFS	1	2.35	1.6	0.08	0.06
		2	2.33	1.4	0.06	0.03
			2.49	1.1	0.11	

[a] Fits performed on $k^3\chi$ using theoretical amplitude and phase shift functions calculated with FEFF 7 from Pb-chalcophanite; theoretical functions were calibrated on αPbO and the threshold energy ΔE was fixed to −1.0 eV by reference to αPbO. Shell = number of fitting shells. σ is the Debye-Waller factor; R_p is the figure of merit of the spectral fit. N_{Free} = 8. For one-shell fits, N_{Float} = 3, and for two-shell fits, N_{Float} = 6.

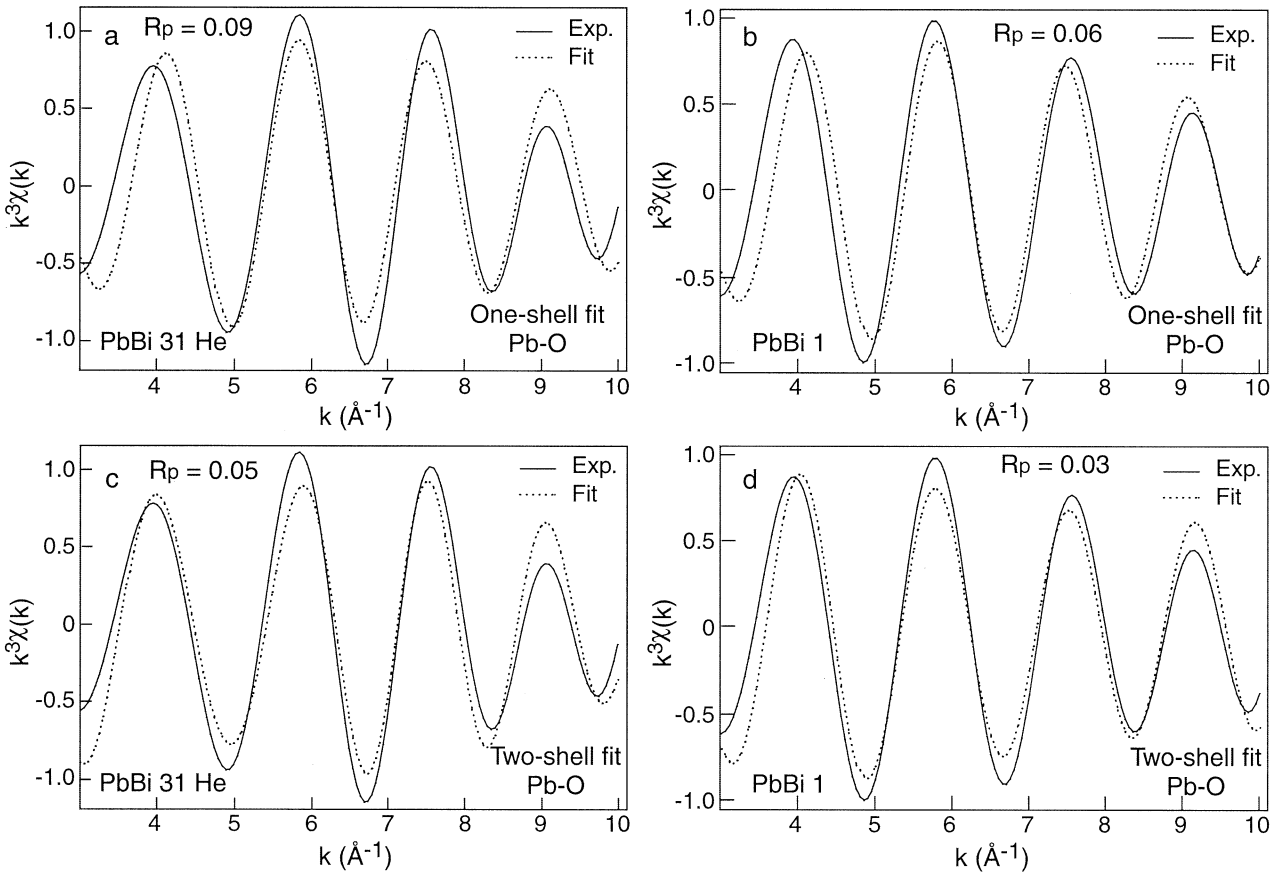

Fig. 16. Experimental Pb-O contributions to EXAFS for a selection of sorption samples (solid lines) and spectral fits (dotted lines). These partial EXAFS spectra were obtained by inverse Fourier transforming (FT^{-1}) first RSF peaks in Fig. 15. (a, b) One-shell fit of oxygen atoms. (c, d) Two-shell fit of oxygen atoms.

perfectly reproduced, and this misfit possibly originates from the lower signal/noise ratio of EXAFS spectra at high *k* values.

The Pb-Pb distance of 4.61 Å is also not structurally realistic. It is not compatible with the formation of polynuclear Pb complexes, or with the precipitation of a Pb oxide, as the range of Pb-Pb separation in these compounds is typically between 3.5 and 3.8 Å (Bargar et al., 1997a). This distance is also not consistent with Pb-Pb pairs on each side of layer vacancy sites (□). Taking a Pb-Mn distance of 3.76 Å for TC interlayer complexes and a Mn-□ separation of 2.84 Å, this ^{TC}Pb-□-^{TC}Pb distance would be typically $2 \times \sqrt{(3.76^2) - (2.84)^2} = 4.93$ Å. In the case of Pb-Mn pairs this calculation leads to $\sqrt{(3.76^2) - (2.84)^2} + \sqrt{(3.53^2) - (2.84)^2} = 4.56$ Å, which reasonably agrees with the experimental d(Pb-Mn) value of 4.61 Å. Therefore, the EXAFS correlation at ~4.6 Å may be tentatively attributed to ^{TC}Pb-^{TC}Mn^{3+}_{inter} pairs. The fact that the dip at ~5 $Å^{-1}$ deepens with increasing Pb content from PbBi1 to PbBi 6 and to PbBi31 is consistent with this interpretation because the more Pb, the more ^{TC}Pb-^{TC}Mn^{3+}_{inter} pairs would be present. However, this structural assignment is not corroborated by XRD results (Part 1), which suggest that only one interlayer cation is sorbed per vacancy because the total number of interlayer cations is equal to the number of $□_{layer}$. Attempts to reconcile EXAFS and XRD interpretations on this point failed.

Sample PbBi 58 does not have a deep dip at ~5 $Å^{-1}$ despite its higher Pb content, and other spectral peculiarities can be seen by eye. Figures 14 and 15 show that this sample has a smaller EXAFS and RSF amplitude and a slightly left-shifted imaginary part. These features are consistent with the presence of some TE interlayer complexes detected by XRD and SAED because, on the basis of the quenselite structure, TE complexes have shorter mean Pb-O and Pb-Mn distances. Although this argument is suggestive, it is inconclusive because spectral fitting showed that only the mean Pb-O distance is reduced in PbBi 58 ($\Delta R \sim 0.04$ Å, Table 4). Therefore, because all Pb-sorbed birnessites have similar average coordination distances, we can say only that the local structure about Pb atoms is more disordered in PbBi 58, and that this finding is consistent with the coexistence of TC and TE complexes in this sample, despite its moderate metal sorption density compared with ZnBi 128 and CuBi 156. All Pb-RSFs have a longer correlation peak near $R + \Delta R = 5$ Å, which was also observed by Matocha et al. (Fig. 5 in Matocha et al., 2001). This peak is at a similar position as peak C in chalcophanite (Fig. 5b) and, on the basis of our P-EXAFS study, it can be attributed to the contribution from next nearest layer Mn atoms (Mn2 shell).

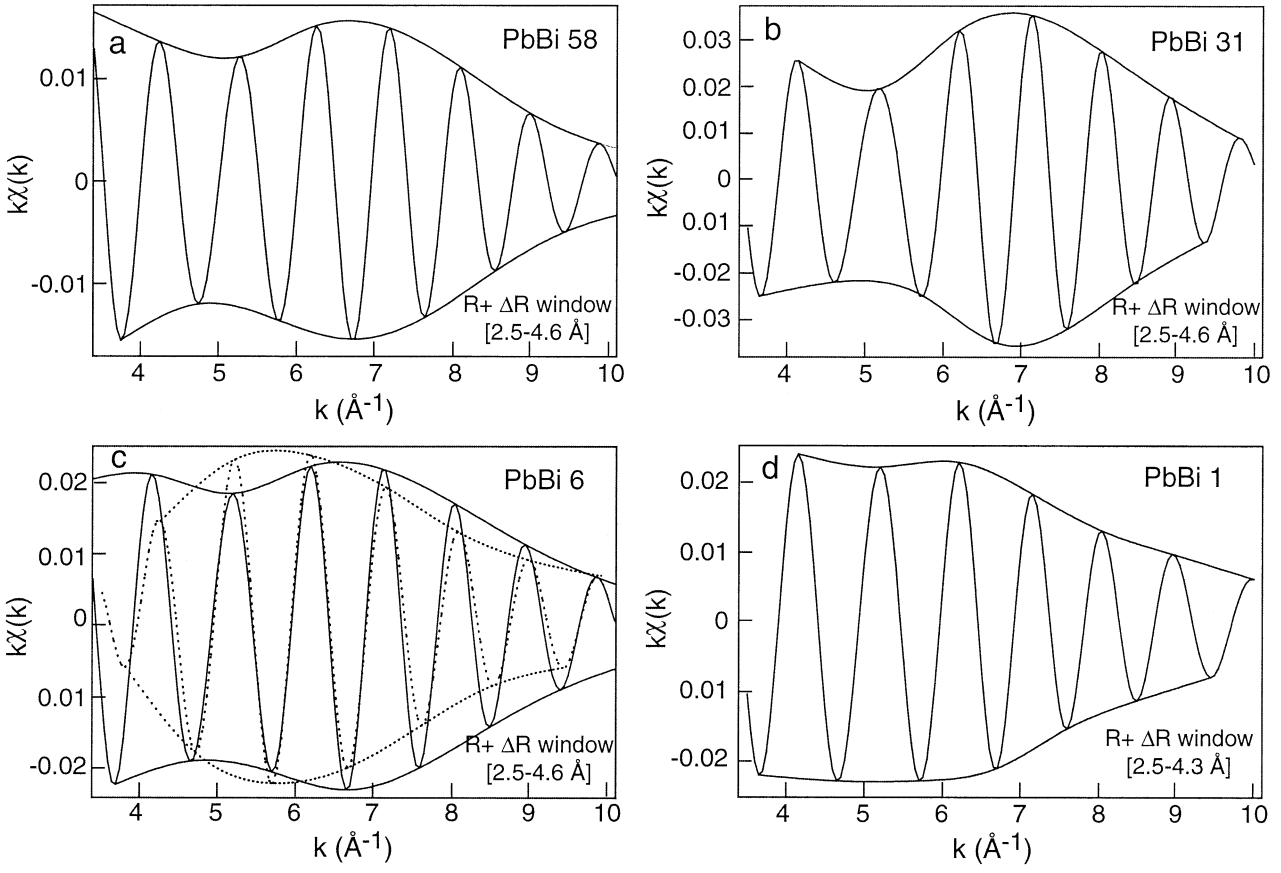

Fig. 17. Cationic shell contributions to EXAFS for PbBi samples. These partial EXAFS spectra were obtained by inverse Fourier transforming second RSF peaks in Fig. 15. The $R + \Delta R$ window of the FT^{-1} is 2.5 to 4.6 Å for (a–c) (solid line); 2.5 to 3.9 Å for (c) (dotted line); and 2.5 to 4.3 Å for (d). When the Fourier transform is performed with a larger $R + \Delta R$ window, a minimum in the amplitude is observed at $\sim$5 $Å^{-1}$, which indicates the presence of two Pb-cationic shells. The valley in the amplitude (i.e., beat node) at $\sim$5 $Å^{-1}$ is deeper at higher Pb concentration. All spectra were reduced the same way, and the deepness of the valley does not arise from variations in the background correction function.

5. DISCUSSION

5.1. Origin of the Structural Disorder around Sorbed Cations

A significant result from this study is the systematic low amplitude of the EXAFS signal for Me-sorbed birnessites. This is illustrated in Figure 19, which compares RSFs for ZnBi 69, CuBi 156, and PbBi 6 to chalcophanite. The displacement of atoms within a shell relative to the mean coordination distance or the multiplicity of unequivalent sorption sites causes a smearing of the interference function and a reduction in the net scattering amplitude. This reduction occurs because the EXAFS interference function $\chi(k)$ consists of a weighted sum of scattering contributions from all coordination shells of atoms surrounding the X-ray absorber in its different crystallographic sites. Three types of disorder were identified in birnessite but are absent in chalcophanite.

The first type is the distortion of Cu and Pb coordination polyhedra as a result of the asymmetry of the outer electronic orbitals of Cu^{2+} and Pb^{2+}. In CuO_6 octahedra, the four planar Cu-O bond lengths are almost equivalent ($\sim$1.95 Å), and the two apical oxygen atoms are typically between 2.2 and 2.4 Å (e.g., Hyde and Anderson, 1989). The increased spread in distance compared with chalcophanite ($d(Zn\text{-}O_{layer})$ = 2.07 Å, $d(Zn\text{-}O_{inter})$ = 2.14 Å) accounts, at least partly, for the drop of peak A in CuBi 156 (Fig. 19). Similarly to quenselite, the static displacement of coordination oxygen atoms is even higher in Pb- than in Cu-sorbed birnessite, and this disorder contributes greatly to the 85% reduction of the first RSF peak observed for PbBi 6. The second type of disorder is the multiplicity of interlayer complexes having different bonding environments. This situation was observed in PbBi (TC and TE complexes) and in ZnBi ($^{[VI]}$TC and $^{[IV]}$TC complexes). The third type of disorder comes from the presence of Mn^{3+} in the MnO_2 layer that separates Mn-Mn distances (Silvester et al., 1997) and also displaces oxygen atoms from their ideal position as a result of the Jahn-Teller distortion of the MnO_6^{9-} octahedron. For instance, Mn^{3+} is bonded to four equatorial O at 1.93 Å and two apical O at 2.26 Å in crednerite ($Cu^{+}Mn^{3+}O_2$; Töpfer et al., 1995), and to four O at 1.90 to 1.98 Å and two O at 2.25 to 2.37 Å in quenselite. As a result of the replacement of some Mn^{4+} by Mn^{3+} in the octahedral layer of birnessite, Me-Mn distances are more variable in this mineral than in chalcophanite (3.49 to 3.50 Å), which is devoid of Mn^{3+}. The structural disorder

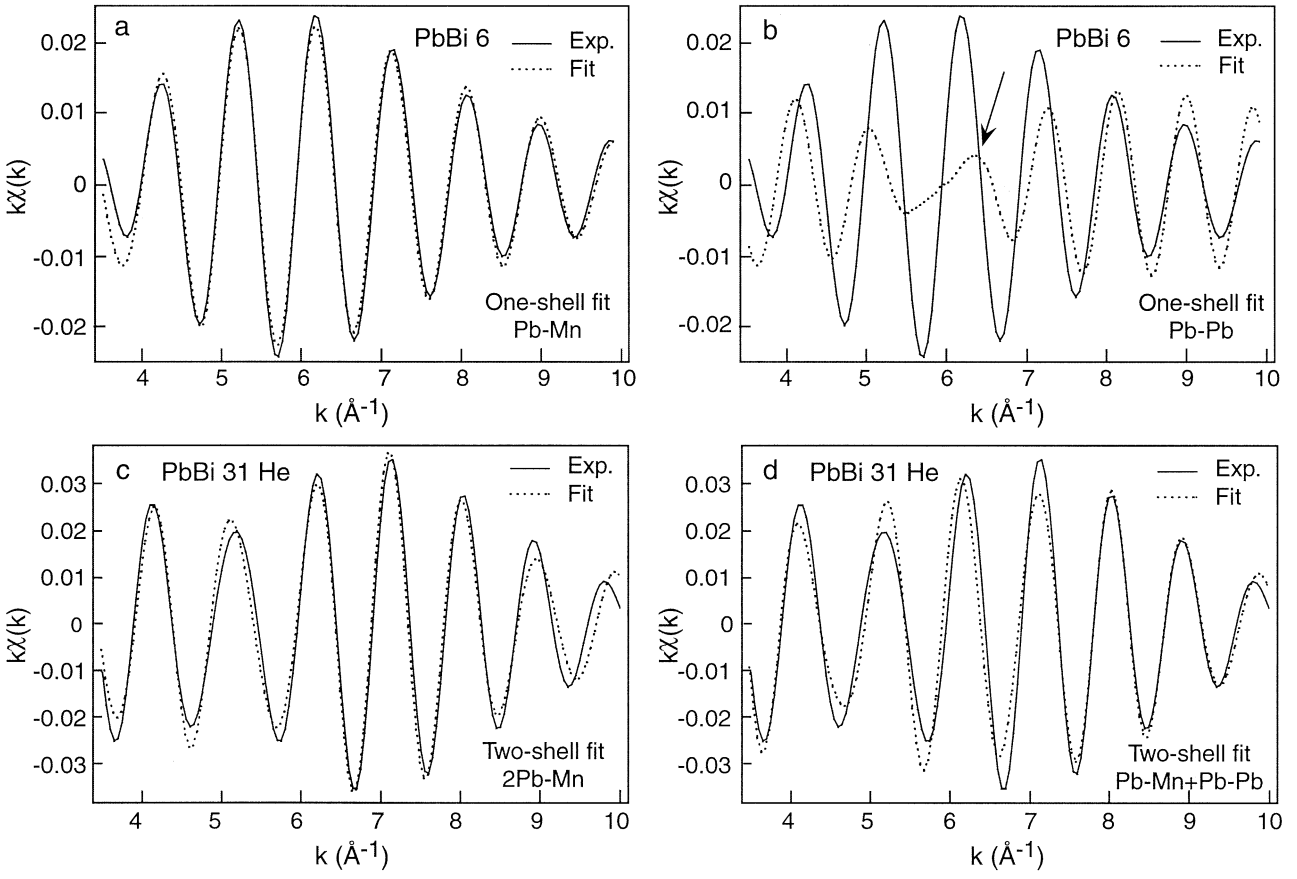

Fig. 18. Experimental cationic shell contributions to EXAFS (solid line) and least squares fits (dotted line) for PbBi 6 and PbBi 31. $R + \Delta R$ window equals 2.5 to 3.9 Å for PbBi 6 and 2.5 to 4.6 Å for PbBi 31.

induced by the nonstoichiometry of the birnessite brucitic layer compounds the two previous types of disorder. Cumulatively, the disorder explains the low amplitude of higher distance RSF peaks (B, C…) for all sorption samples (Fig. 19). The explanation of the low amplitude of peak B in MeBi is reinforced by the results of Manceau et al. (1997) on the oxidation of Co^{2+} by birnessite, which showed that the symmetry of the MnO_2 layer, and hence the amplitude of the EXAFS signal, increases when the amount of Mn_{layer}^{3+} decreases and the amount of Mn_{layer}^{4+} concomitantly increased after the Co^{2+} to Co^{3+} oxidation.

Table 5. EXAFS parameters for Pb-(Mn, Pb) pairs.[a]

Sample	Shell	Atom	R (Å)	N	σ (Å)	R_p
PbBi 58	2	Mn	3.78	1.1	0.10	0.011
		Mn	4.61	0.7	0.10[b]	
PbBi 31RT	2	Mn	3.78	1.7	0.11	0.012
		Mn	4.62	1.1	0.11[b]	
PbBi 31He	2	Mn	3.80	1.7	0.08	0.013
		Mn	4.61	1.3	0.08[b]	
PbBi 6	2	Mn	3.80	1.6	0.10	0.014
		Mn	4.62	1.0	0.10[b]	
PbBi 1	2	Mn	3.78	1.9	0.11[b]	0.007
		Mn	4.59	0.9	0.11[b]	

[a] Fits performed on $k\chi$ using theoretical amplitude and phase shift functions calculated with FEFF 7 from a Pb-chalcophanite model. Shell = number of fitting shells. Atom is the nature of backscatter; σ is the Debye-Waller factor; R_p is the figure of merit of the spectral fit.

[b] σ values held identical in the two shells. $N_{Free} = 9$ and $N_{Float} = 5$.

5.2. Relative Stability of $^{[VI]}$Zn and $^{[IV]}$Zn Interlayer Complexes

One of the most important findings from EXAFS spectroscopy is the unexpected formation of $^{[IV]}$Zn interlayer complexes at low to intermediate surface coverage on the same crystallographic site as $^{[VI]}$Zn in chalcophanite. The $^{[IV]}$Zn coordination geometry was even less expected because XRD showed that Mn layers are shifted by $+a/3$ in Zn-sorbed birnessite as in chalcophanite, and not orthogonally stacked as in HBi (Lanson et al., 2002a). Therefore, birnessite particles likely have some specific structural features that prevent them from transforming completely into chalcophanite. As will be shown below, the reason for the stabilization of $^{[IV]}$Zn complexes in the interlayer region of birnessite is the presence of Mn_{layer}^{3+}, which markedly decreases the Pauling bond strength of O_{layer} atoms. The following discussion is divided into three parts. Because the chalcophanite structure is fairly well-known, and because this phyllomanganate is ideally devoid of Mn^{3+} cations, the valence of all its chemical bonds will be calculated

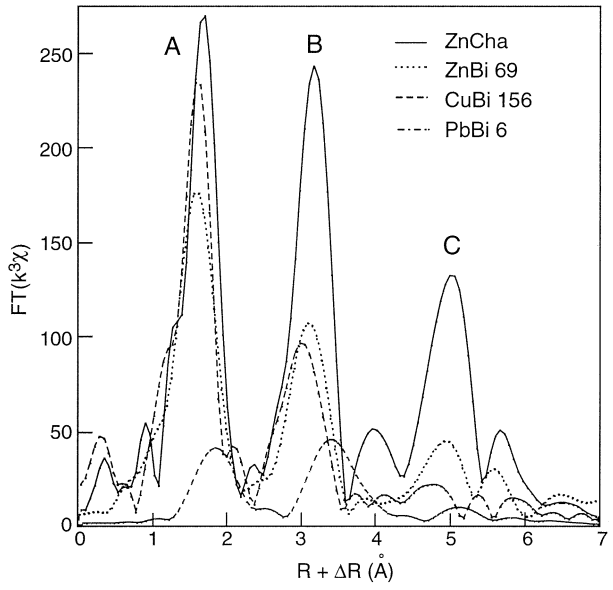

Fig. 19. Comparison of RSFs for chalcophanite (Zn K-edge), Zn sorbed birnessite (ZnBi 69, Zn K-edge), Cu sorbed birnessite (CuBi 156, Cu K-edge) and Pb sorbed birnessite (PbBi 6, L_3-edge). The reduced amplitude of RSF peaks in sorption samples reflect an increase of structural disorder compared with the stoichiometric phyllomanganate chalcophanite. The disorder includes the replacement of some Mn^{4+} by Mn^{3+} in the octahedral layer of birnessite, the mixture of interlayer sorbate species (e.g., $^{[IV]}$Zn and $^{[VI]}$Zn, and Pb TE [triple edge] and TC [triple corner] interlayer complexes), and the distortion of sorbate polyhedra (Cu and Pb) caused by the strong asymmetry of electronic orbitals for Cu^{2+} (Jahn-Teller distortion) and Pb^{2+} (stereoactive lone pairs of $6s^2$ electrons).

first. How Mn^{3+} for Mn^{4+} substitutions affect individual bond-valences in the chalcophanite structure then will be considered. Finally, it will be shown that the tetrahedral coordination provides a better charge balance of O_{layer}, and also O_{adj} via the formation of strong hydrogen bonds.

To determine the Pauling bond strength (Brown, 1981) of atomic pairs in chalcophanite, calculations of empirical bond-valences were performed by using the structural model of Post and Appleman (1988) and the parameter values (r_0) for the bond valence–bond distance correlation functions, $s = \exp[(r_0 - r)/0.37]$, given by Brese and O'Keefe (1991). The incident bond-valence sum for each atom in the asymmetric unit cell of chalcophanite is listed in Table 6. Summations at each position (Fig. 20a) agree well with the expected formal valence +4 for Mn, +2 for Zn, and −2 for O(1) but less well for O(2) (1.89 v.u.), O(3) (1.87 valence units, v.u.), O(4) = O_{inter} (2.20 v.u.), H(1) (1.11 v.u.) and H(2) (0.88 v.u.).

Table 6. Bond-valence values (v.u.) for the XRD structural model of chalcophanite.[a]

Variable	Zn	Mn	H(1)	H(2)	Sum
O(1)		0.56, 0.65, 0.69		0.04	1.94
O(2)	0.37 × 3 ↓	0.73, 0.75	0.04		1.89
O(3)		0.61 ± 3→	0.01_5 × 3→		1.87
O(4)	0.31 × 3 ↓		1.05	0.77, 0.07	2.20
Sum	2.04	3.99	1.11	0.88	

[a] Calculated using the parameters of Brese and O'Keefe (1991). The arrows show which sum (vertical vs. horizontal) the multiplicative factor is for.

A better charge balance for O(4) and O(2) can be obtained by lengthening the Zn-O(4) bond and shortening the Zn-O(2), that is, by moving Zn toward the Mn layer. New atomic coordinates were least squares refined so that the calculated bond-valence sum for each atom matches, as best as possible, its formal charge. The optimization procedure was performed by the distance and valence least squares (DVLS) program (Kroll et al., 1992). Unit cell parameters and space group were constrained to their XRD determinations (Post and Appleman, 1988). Mn-O distances were weighted at 4 to their XRD values, and Zn-O distances were weighted at 10 to their EXAFS values (2.04 and 2.16 Å). All other interatomic distances were unweighted. For symmetry reasons, only fractional coordinates were refined. The minimization converged to the same coordinates regardless of their initial values, which engenders confidence in the calculation. No marked differences in atomic positions between the XRD and the DVLS models were obtained, but the overall electroneutrality of atoms in the structure is substantially better in the simulated model (Table 7). The DVLS model was also tested for correctness by comparison of X-ray structure factors: the DVLS and XRD structural models differed by a residual *R* index of 3.9% as compared with a difference of 4% between the experimental pattern and the XRD model obtained by Rietveld refinement (Post and Appleman, 1988).

In the DVLS model, the O(4) atom has an incident bond-valence sum of 2.07 v.u. coming from the Zn-O(4) bond (0.29 v.u), two O-H bonds (0.81, 0.90 u.v.), and from the H(2)-O(4) H-bond (0.07) with a nearby H_2O molecule (Fig. 20b,c; Table 8). The O(2) has a bond-valence sum of 1.94 v.u., coming from two Mn-O(2) bonds (0.74, 0.76 v.u.), the Zn-O(2) bond (0.40 v.u.), and the H(1)-O(2) H-bond (0.05 v.u., interlayer H-bond). Therefore, both the XRD and DVLS minimizations of the chalcophanite structure lead to an undersaturation of O(2), and any replacement of Mn^{4+} by Mn^{3+} in the birnessite layer shall increase this charge deficit. The excess of negative charge at O(2) can be balanced by the formation of a four- over six-fold coordinated Zn interlayer complex because in undistorted polyhedra, Zn provides ideally 2+/4 = 0.5 charges in fourfold vs. 2+/6 = 0.33 charges in sixfold coordination.

Mn^{3+}-O bond lengths are typically between 1.92 and 2.37 Å in pure Mn^{3+}-phyllomanganates (Rouse, 1971; Töpfer et al., 1995) and the strong asymmetry of MnO_6^{9-} octahedra prevents calculating the bond valence incident at O(2) because the orientation of individual bonds in the Mn layer are unknown. However, an estimate can be made by taking undistorted Mn^{3+} and Mn^{4+} polyhedra. The ideal bond valence sum of O(2) for the $2^{[VI]}Mn^{4+}$-O(2)-$^{[VI]}$Zn configuration is $2x(4+/6) + (2+/6) = 1.66$ v.u., and is identical to that for the ($^{[VI]}Mn^{4+} + {}^{[VI]}Mn^{3+}$)-O(2)-$^{[IV]}$Zn configuration: (4+/6) + (3+/6) + (2+/4) = 1.66 v.u (Fig. 20e). Therefore, the excess of negative charge at O(2) resulting from the presence of Mn^{3+} in birnessite layer is, on average, perfectly balanced by the formation of $^{[IV]}ZnO_4$ complexes above vacancies. According to this interpretation, each O(2) bonded to a $^{[IV]}ZnO_4$ complex would be shared by one Mn^{3+} and one Mn^{4+} octahedron and, consequently, each $^{[IV]}$Zn would be ideally neighbored by $3Mn^{4+}$

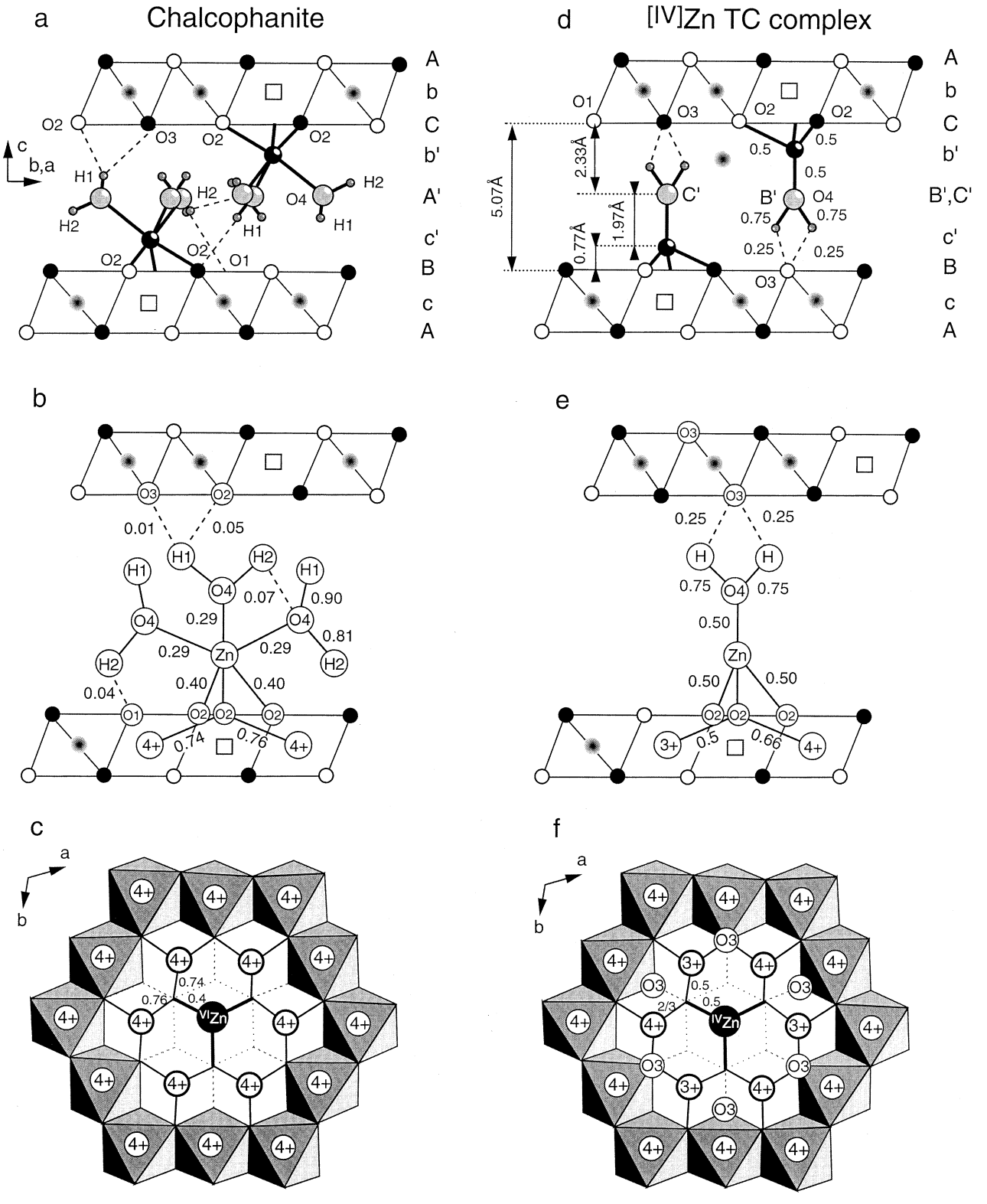

Fig. 20. Interlayer structure and bond valence calculation for the DVLS model of chalcophanite (left column), and for [IV]Zn-sorbed birnessite (TC interlayer complex, right column).

Table 7. Atomic positions for chalcophanite according to XRD and DVLS refinements.

	XRD[a]			DVLS[b]		
Element	*x*	*y*	*z*	*x*	*y*	*z*
Zn	0	0	0.099975	0	0	0.098200
Mn	0.718691	0.577711	0.999483	0.718061	0.578271	0.999328
O(1)	0.527845	0.622975	0.047212	0.527988	0.623964	0.047143
O(2)	0.260775	0.206555	0.050482	0.258820	0.203855	0.049833
O(3)	0	0	0.712503	0	0	0.710095
O(4)	0.179006	0.931076	0.164352	0.178416	0.928151	0.163738
H(1)	0.229000	0.025000	0.198000	0.230066	0.027122	0.199844
H(2)	0.310000	0.940000	0.144000	0.307989	0.939221	0.143618

[a] From Post and Appleman (1988).
[b] This study.

and $3Mn^{3+}$, as illustrated in Fig. 20f. Consistent with this hypothesis, XRD and chemical analysis showed that at high Zn loading (ZnBi 122 and ZnBi 128) the Mn^{3+} to $^{[IV]}Zn$ ratio is close to three (Lanson et al., 2002a).

In chalcophanite, the 2.00–1.66 = 0.34 v.u. charge deficit at O(2) is compensated by (1) shortening of the three $^{[VI]}Zn$- O(2) and elongation of the three $^{[VI]}Zn$-O(4) bonds (gain of 0.4 − 2/6 = 0.07 v.u.), (2) shortening of the Mn^{4+}-O(2) distance (gain of 0.75–4/6 = 0.09 v.u.), and (3) by the H(1)-O(2) interlayer H-bond (0.05 v.u.). But the first and third of these mechanisms are absent in the ($^{[VI]}Mn^{4+}$ + $^{[VI]}Mn^{3+}$)-O(2)-$^{[IV]}Zn$ configuration because the unique $^{[IV]}Zn$-O(4) bond cannot be elongated much to compensate a shortening of the three $^{[IV]}Zn$-O(2) bonds and the H(1)-O(2) H-bond no longer exists. Therefore, the undersaturation of O(2) coordinated to $^{[IV]}Zn$ has to be substantially compensated by increasing the Mn^{3+}-O(2) bond strength, that is by orienting two of the four short Mn^{3+}-O bonds of the Jahn-Teller distorted MnO_6^{9-} octahedra toward the vacancy, and the two longest bonds outward. As a result, six O_{layer} atoms coordinated to three Mn octahedra become undersaturated (O(3) in Fig. 20f). It is shown below that this charge deficit is readily compensated by the $+a/3$ displacement of successive layers.

Phyllomanganate layers are held together by (1) weak electrostatic attractions between the interlayer cation and the next O_{layer}, (2) hydrogen bonds between OH_{inter} and O_{layer}, and van der Waals forces. In chalcophanite, $^{[VI]}Zn$ is coordinated to three H_2O groups (O(4) atoms) of which one hydrogen (H1) bonds with two oxygen atoms (O(2) and O(3)) of the adjacent layer (Figs. 20a,b). The O(4)-O(2) and O(4)-O(3) separations are relatively long (2.98 Å and 3.12 Å, respectively), and successive Mn layers thus appear to be weakly bonded by hydrogen-bonds ((0.05 + 0.015) × 3 ~ 0.2 v.u. per Zn atom, Table 8), leaving predominantly van der Waals forces to maintain the cohesion between the O_{layer} and H_2O sheets. When Zn is fourfold coordinated, the stacking mode between successive anionic and cationic sheets becomes AcBc'C'CbAb'B'BaC and AcBB'b'CbAA'a'BaC (Fig. 20d) compared with AcBc'A'b'CbAb'C'a'BaC in chalcophanite (Fig. 20a), meaning that the apical water molecule (O(4)) coordinated to $^{[IV]}Zn$ is aligned along the c* direction with the O(3) atom of the next layer (a'A'A, b'B'B and c'C'C sequences in the symbolic notation). The O(4)-O(3) distance in Zn-sorbed birnessite can be calculated from its interlayer spacing (5.07 Å; Lanson et al., 2002a), the elevation of Zn from the O_{layer} sheet (0.77 Å, Fig. 9c), and the d($^{[IV]}Zn$-O) distance (1.97 Å) (Fig. 20d). This calculation yields an O(4)-O(3) distance of 2.33 Å, which is short for H-bonding (Brown, 1976) but crystallochemically plausible. The bond-valence model for the interlayer structure of $^{[IV]}ZnBi$ obtained for this structural configuration is presented in Figures 20d and 20e. As expected from the shortness of the O(4)-O(3) distance, the strength of the H-O(3) hydrogen bond is high ~0.25 v.u. Of course, this is a maximum value because in real structures the $^{[IV]}Zn$-O(4)-(O3) vector can be bent, thus relaxing the strain of the O(4)-O(3) pair. Therefore, the $+a/3$ stacking mode together with the formation of $^{[IV]}Zn$ complexes allow the formation of strong hydrogen bonds with O(3) atoms of the adjacent layer. The bond valence strength sums up to ~0.5 v.u. and, amazingly, equals the $^{[IV]}Zn$-O(2) bond-valence on the other side of the interlayer space (Fig. 20e).

The formation of strong H-O(3) hydrogen bonds in ZnBi indicates that the O(3) atom of the adjacent layer is greatly undersaturated with respect to Pauling valence strengths, and suggests that this oxygen is shared by two Mn^{4+} and one Mn^{3+} octahedra (Fig. 20f). As discussed previously, simple crystal chemical considerations show that the bond-valence requirement of O(3) can be readily satisfied by assuming that one of the two long Mn^{3+}-O bonds from the Jahn-Teller distorted MnO_6^{9-} octahedron points toward O(3), which is consistent with the formation of a short equatorial Mn^{3+}-O(2) bond. According to this structural model, the two Mn^{+4}-O(3) bonds ideally would contribute (4/6)x2 = 1.33 v.u., the two H-bonds,

Table 8. Bond-valence values (v.u.) for the DVLS structural model of chalcophanite.[a]

Variable	Zn	Mn	H(1)	H(2)	Sum
O(1)		0.56, 0.65, 0.69		0.04	1.94
O(2)	0.40 × 3 ↓	0.74, 0.76	0.05		1.94
O(3)		0.64 × 3→	0.01_5 × 3→		1.96
O(4)	0.29 × 3 ↓		0.90	0.81, 0.07	2.07
Sum	2.07	4.04	0.96	0.92	

[a] Calculated using the parameters of Brese and O'Keefe (1991). The arrows show which sum (vertical vs. horizontal) the multiplicative factor is for.

0.5 v.u., and a d(Mn^{3+}-O) distance of 2.41 Å, 0.17 v.u., summing to 2 v.u. Finally, it is concluded that $^{[IV]}$Zn in monoclinic birnessite most likely results from Mn^{3+} for Mn^{4+} substitutions in the octahedral layer, because this complex offers a better layer charge compensation than $^{[VI]}$Zn. Therefore, the absence of $^{[IV]}$Zn in chalcophanite is consistent with its lack of heterovalent Mn cations.

5.3. Distribution of $^{[IV]}$Zn and $^{[VI]}$Zn Complexes

We have seen in the previous section that $^{[IV]}$Zn complexes are likely surrounded by $3Mn^{3+}$ and $3Mn^{4+}$, and that this local order results in the undersaturation (~ -0.5 v.u.) of six oxygen atoms (noted O(3) in Fig. 20e,f), three of which belong to the lower, and three to the upper O sheet of a given MnO_2 layer. To compensate the negative charge of the O(3) atoms of a given layer, the next and previous adjacent layers should have each three vacancies located above or below the O(3) atoms, as represented in projection in Fig. 20e for O(3) of the lower sheet. Consequently, the formation of a layer vacancy capped by a $^{[IV]}ZnO_4$ tetrahedron induces the formation of three holes in the next layer and so on, because only in this case can each undersaturated oxygen atom obtain its missing $+0.5$ v.u. from the H_2O molecule coordinated to $^{[IV]}$Zn. Thus, the formation of $^{[IV]}$Zn-capped vacancies leads to the formation of three dimensional clusters, in which Mn^{3+}_{layer}, vacant sites, and interlayer $^{[IV]}$Zn are segregated. The cluster size should be determined by the amount of available interlayer Zn and Mn^{3+} in a given layer. Although speculative, this model is consistent with two experimental results. First, it provides a straightforward explanation to the preferential formation of $^{[IV]}$Zn over $^{[VI]}$Zn complexes at low Zn loading. Initially, there are many available Mn^{3+}_{layer}, and therefore there is no limitation to cluster formation. With increasing Zn loading, the amount of available Mn^{3+}_{layer} decreases, and the formation of chalcophanite-like local environments containing $^{[VI]}$Zn complexes surrounded by 6 Mn^{4+}_{layer} is favored. Second, in ZnBi 128 (Zn/Mn = 0.128) $\sim$25% of Zn is fourfold coordinated, and the theoretical amount of Mn^{3+} per Mn obtained by this model ($3 \times 0.128/4 = 0.096$) is close to the fractional amount of Mn^{3+} in the structural formula (0.104; Lanson et al., 2002a).

Segregation of $^{[IV]}$Zn complexes is probably intraparticular otherwise some birnessite particles would be Mn^{3+}-free, and we know they are not from selected area electron diffraction (SAED) results (Drits et al., 1997). However, because all birnessite particles do not have the same layer charge (the distribution is ideally bimodal as discussed by Silvester et al., 1997), their $^{[IV]}$Zn/$^{[VI]}$Zn content ought to vary. Finally, the relationship between the local domain structure of $^{[IV]}$Zn discussed here, and the two-dimensional (particles of type 1 and 2) and one-dimensional (particles of type 3) Zn ordering observed by electron diffraction in Part 2 (Drits et al., 2002), is unclear. However, it is interesting to note that both approaches, electron diffraction and EXAFS spectroscopy coupled with bond valence considerations, suggest a segregation of $^{[IV]}$Zn and $^{[VI]}$Zn interlayer species and, consequently, of Mn^{3+} and Mn^{4+} in the layer. Drits et al. (2002) attributed the two first types of SAED patterns to chalcophanite particles ($^{[VI]}$Zn clusters), and the third type to particles containing ordered rows of $^{[IV]}$Zn, but more work is needed to close the gap between these long-range (SAED) and short-range (EXAFS, bond valence) structural models.

5.4. Specific Structural Features of Me-Sorbed Birnessite Compared with Chalcophanite

In the literature, the structure of hexagonal birnessite, and more systematically that of metal-sorbed birnessite, has been generally thought to be similar to chalcophanite. This comparison is relevant because these two minerals have in common several important features, namely a large and similar amount of vacant sites in their octahedral layers (one out of six vs. one out of seven, respectively), a similar basal spacing ($\sim$7.2 Å vs. 6.9 Å) related to the presence of a single layer of water in their interlayer space, and the presence of octahedrally coordinated interlayer cations (Mn or Me in Bi vs. Zn in ZnCh) above vacant octahedral sites (TC complex). The combination of four complementary structural techniques (X-ray and electron diffraction in Parts 1 and 2 of this series of articles, and powder and polarized EXAFS spectroscopy in this study) has enabled us to elucidate some of the structural specificities of metal-sorbed birnessite. They include the two following points.

(1) In ZnBi, octahedral holes can be capped not only by $ZnO_3(H_2O)_3$ octahedra as in chalcophanite, but also by ZnO_3H_2O tetrahedra ($^{[VI]}$TC and $^{[IV]}$TC complexes). Interlayer species (such as Pb) can occupy tetrahedral sites delimited by three Mn_{layer} octahedra (TE complex), as in quenselite ($PbMnO_2OH$).

(2) Successive octahedral layers are not necessarily translated by $+a/3$ (monoclinic stacking) in Me-sorbed birnessite as in chalcophanite, but can be also hexagonally stacked, depending on the interlayer cation and presumably on the protocol followed to sorb the metal.

It has been argued in this article that a clue to the different structural features between metal-sorbed birnessite and chalcophanite is the replacement of $\sim$13% of Mn^{4+} by Mn^{3+} in the octahedral layers of birnessite. The additional layer charge deficit created by this substitution can be balanced by forming fourfold coordinated Zn complexes, strong H-bonds between successive layers, and TE complexes in addition to TC complexes. All of these structural adjustments account for the significant structural disorder systematically observed in all Me-sorbed birnessites. Finally, it should be mentioned that the $^{[IV]}$TC Zn interlayer complex observed at low surface coverage on synthetic birnessite has been recently found in soil birnessite (Manceau et al., 2000).

Acknowledgments—We thank Agnès Traverse on beamline D42 at LURE (Orsay) and Jean Louis Hazemann and Olivier Proux on beamline BM32 at the ESRF (Grenoble) for their support during the EXAFS measurements; three anonymous reviewers for their comments; and the two synchrotron facilities for the provision of beam time. V.A.D. is grateful to the Environmental Geochemistry Group of the LGIT at Grenoble and to the Russian Science Foundation for financial support. B.L. and A.M. acknowledge financial support from CNRS/ACI "Eau et Environnement," INSU/Géomatériaux, and CNRS/PICS 709 programs.

Associate editor: D. L. Sparks

REFERENCES

Albertsson J., Abrahams S. C., and Kvick A. (1989) Atomic displacement, anharmonicity, thermal vibration, expensivity and pyroelectric thermal dependences in ZnO. *Acta Cryst.* **B45,** 34–40.

Axe L., Tyson T., Trivedi P., and Morrison T. (2000) Local structure analysis of strontium sorption to hydrous manganese oxide. *J. Colloid Interf. Sci.* **224,** 408–416.

Bardossy G. and Brindley G. W. (1978) Rancieite associated with a karstic bauxite deposit. *Am. Miner.* **63,** 762–767.

Bargar J. R., Brown G. E., and Parks G. A. (1997a) Surface complexation of Pb(II) at oxide-water interfaces: I. XAFS and bond-valence determination of mononuclear and polynuclear Pb(II) sorption products on aluminum oxides. *Geochim. Cosmochim. Acta* **61,** 2617–2637.

Bargar J. R., Brown G. E., and Parks G. A. (1997b) Surface complexation of Pb(II) at oxide-water interfaces: II. XAFS and bond-valence determination of mononuclear and polynuclear Pb(II) sorption products on iron oxides. *Geochim. Cosmochim. Acta* **61,** 2639–2652.

Brese N. E. and O'Keefe M. (1991) Bond-valence parameters for solids. *Acta Cryst.* **B47,** 192–197.

Brigham E. O. (1974) *The Fast Fourier Transform*. Prentice-Hall.

Brouder C. (1990) Angular dependence of X-ray absorption spectra. *J. Phys. Cond. Matter.* **2,** 701–738.

Brown I. D. (1976) On the geometry of O-HO hydrogen bonds. *Acta Cryst.* **A32,** 24–31.

Brown I. D. (1981) The bond-valence method: An empirical approach to chemical structure and bonding. *Structures and Bonding in Crystals* In: (eds. M. O'Keefe and A. Navrotsky), 1–30. Academic Press.

Burns R. G. (1976) The uptake of cobalt into ferromanganese nodules, soils, and synthetic manganese (IV) oxides. *Geochim. Cosmochim. Acta* **40,** 95–102.

Chukhrov F. V. and Gorshkov A. I. (1981) Iron and manganese oxide minerals in soils. *Trans. R. Soc. Edinburgh Earth Sci.* **2,** 195–200.

Chukhrov F. V., Sakharov B. A., Gorshkov A. I. , Drits V. A., and Dikov Y. P. (1985) Investiya Akademie Naukia, SSSR, Seriya GeologicheskayaCrystal structure of birnessite from the Pacific Ocean. *Intern. Geol. Rev.* **27,** 1082–1088 8, 66–73.

Crozier E. D., Rehr J. J., and Ingalls R. (1988) Amorphous and liquid systems. *X-ray Absorption. Principles, Applications, Techniques of EXAFS, SEXAFS, and XANES* In: (eds. D. C. Koningsberger and R. Prins), 373–442. Wiley.

d'Antonio P. and Santoro A. (1980) Powder neutron diffraction study of chemically prepared beta lead dioxide. *Acta Cryst.* **B36,** 2394–2397.

Dillard J. G., Koppelman M. H., Crowther D. L., Schenk C. V., Murray J. W., and Balistrieri L. (1981) X-ray photoelectron spectroscopic (XPS) studies on the chemical nature of metal ions adsorbed on clays and minerals. *Adsorption from Aqueous Solutions* In: (ed. P. H. Tewari), 227–240. Plenum Press.

Dillard J. G., Crowther D. L., and Murray J. W. (1982) The oxidation states of cobalt and selected metals in Pacific ferromanganese nodules. *Geochim. Cosmochim. Acta* **46,** 755–759.

Dixon J. B. and Skinner H. C. W. (1992) Manganese minerals in surface environments. *Biomineralization Processes of Iron and Manganese: Modern and Ancient Environments* In: (eds. H. C. W Skinner and R. W. Fitzpatrick), 31–50. CATENA Verlag.

Douglas B., McDaniel D., and Alexander J. (1994) *Concepts and Models of Inorganic Chemistry*. Wiley.

Drits V. A., Silvester E., Gorshkov A. I., and Manceau A. (1997) The structure of synthetic monoclinic Na-rich birnessite and hexagonal birnessite. Part 1. Results from X-ray diffraction and selected area electron diffraction. *Am. Miner.* **82,** 946–961.

Drits V. A., Lanson B., Bougerol-Chaillout C., Gorshkov A. I., Manceau A. (2002) Structure of heavy metal sorbed birnessite. Part 2. Results from electron diffraction. *Am. Minerol.* In press.

Gadde R. R. and Laitinen H. A. (1974) Studies of heavy metals adsorption by hydrous iron and manganese oxides. *Anal. Chem.* **46,** 2022–2026.

Galy J., Meunier G., Andersson S., and Astrom A. (1975) Stéréochimie desélément comportant des paires non liées: Ge(II), As(III), Se(IV), Br(V), Sn(II), Sb(III), Te(IV), I(V), Xe(VI), Tl(I), Pb(II), et Bi(III) (oxydes, fluorures et oxyfluorures). *J. Solid State Chem.* **13,** 142.

Giovanoli R. (1980) On natural and synthetic manganese nodules. *Geology and Geochemistry of Manganese* In: (eds. I. M. Varentsov and G. Grasselly), 160–210. Hungarian Academy of Science.

Glover E. D. (1977) Characterization of a marine birnessite. *Am. Miner.* **62,** 278–285.

Goldberg E. D. (1965) Minor elements in sea-water. *Chemical Oceanography* In: (eds. J. P. Riley and G. Skirrow), 163–196. Academic Press.

Heald S. M. and Stern E. A. (1977) Anisotropic X-ray absorption in layered compounds. *Phys. Rev.* **B16,** 5549–5559.

Hem J. D. (1978) Redox processes at surfaces of manganese oxide and their effects on aqueous metal ions. *Chem. Geol.* **21,** 199–218.

Hill R. J. (1985) The structure of loseyite. *Acta Cryst.* **C41,** 1281–1284.

Huang P. M. (1991) Kinetics of redox reactions on manganese oxides and its impact on environmental quality. *Rates of Soil Chemical Processes* In: (eds. D. L. Sparks and D. L. Suarez), 191–230. Soil Science Society of America.

Hyde B. G. and Anderson S. (1989) *Inorganic Crystal Structures*. Wiley.

Jenne E. A. (1967) Controls on Mn, Fe, Co, Ni, Cu and Zn concentrations in soils and water: The significant role of hydrous Mn and Fe oxides. *Trace Inorganics in Water* In: (ed. R. F. Gould), 337–387. American Chemical Society, Washington, Advances in chemistry series, Vol. 73.

Kroll H., Maurer H., Stöckelmann D., Beckers W., Fulst J., Krüsemann R., Stutenbäumer T., and Zingel A. (1992) Simulation of crystal structures by a combined distance–least-squares/valence-rule method. *Zeit. Krist.* **199,** 49–66.

Lanson B., Drits V. A., Silvester E. J., and Manceau A. (2000) Structure of H-exchanged hexagonal birnessite and its mechanism of formation from. Na-rich monoclinic buserite at low pH: New data from X-ray diffraction. *Am. Miner.* **85,** 826–835.

Lanson B., Drits V. A., Gaillot A. C., Silvester E., Plancon A., Manceau A. (2002a) Structure of heavy metal sorbed birnessite. Part 1. Results from X-ray diffraction, *Am. Minerologist.* In press.

Lanson B., Drits V. A., Feng Q., Manceau A. (2002b) Structure of synthetic Na-rich birnessite: Evidence for a triclinic one-layer cell. *Am. Minerologist*. In press.

Lengeler B. and Eisenberger P. (1980) Extended X-ray absorption fine structure analysis of interatomic distances, coordination numbers, and mean relative displacements in disordered alloys. *Phys. Rev.* **B21,** 4507–4528.

Leroux F., Le Gal La Salle A., Guyomard D., and Piffard Y. (2001) Interleaved oxovanadium cations in the rancieite manganese oxideδ-MnO_2. *J. Mater. Chem.* **11,** 652–656.

Ma Y., Suib S. L., Ressler T., Wong J., Lovallo M., and Tsapatsis M. (1999) Synthesis of porous CrO_x pillared octahedral layered manganese oxide materials. *Chem. Mater.* **11,** 3545–3554.

Manceau A. (1995) The mechanism of anion adsorption on Fe oxides: Evidence for the bonding of arsenate tetrahedra on free $Fe(O,OH)_6$ edges. *Geochim. Cosmochim. Acta* **59,** 3647–3653.

Manceau A. and Combes J. M. (1988) Structure of Mn and Fe oxides and oxyhydroxides: A topological approach by EXAFS. *Phys. Chem. Miner.* **15,** 283–295.

Manceau A., Bonnin D., Kaiser P., and Frétigny C. (1988) Polarized EXAFS of biotite and chlorite. *Phys. Chem. Miner.* **16,** 180–185.

Manceau A., Bonnin D., Stone W. E. E., and Sanz J. (1990) Distribution of Fe in the octahedral sheet of trioctahedral micas by polarized EXAFS. Comparison with NMR results. *Phys. Chem. Miner.* **17,** 363–370.

Manceau A., Charlet L., Boisset M. C., Didier B., and Spadini L. (1992) Sorption and speciation of heavy metals on Fe and Mn hydrous oxides. From microscopic to macroscopic. *Appl. Clay Sci.* **7,** 201–223.

Manceau A., Boisset M. C., Sarret G., Hazemann J. L., Mench M., Cambier P., and Prost R. (1996) Direct determination of lead speciation in contaminated soils by EXAFS spectroscopy. *Environ. Sci. Technol.* **30,** 1540–1552.

Manceau A., Drits V. A., Silvester E., Bartoli C., and Lanson B. (1997) Structural mechanism of Co(II) oxidation by the phyllomanganate, Na-buserite. *Am. Miner.* **82,** 1150–1175.

Manceau A., Chateigner D., and Gates W. P. (1998) Polarized EXAFS, distance-valence least-squares modeling (DVLS) and quantitative texture analysis approaches to the structural refinement of Garfield nontronite. *Phys. Chem. Miner.* **25,** 347–365.

Manceau A., Schlegel M., Chateigner D., Lanson B., Bartoli C., and Gates W. P. (1999a) Application of polarized EXAFS to fine-grained layered minerals. *Synchrotron X-ray Methods in Clay Science* In:

(eds. D. Schulze, P. Bertsch, and J. Stucki), 68–114. Clay Mineral Society of America.

Manceau A., Schlegel M., Nagy K. L., and Charlet L. (1999b) Evidence for the formation of trioctahedral clay upon sorption of Co^{2+} on quartz. *J. Coll. Interf. Sci.* **220,** 181–197.

Manceau A., Lanson B., Schlegel M. L., Hargé J. C., Musso M., Eybert-Bérard L., Hazemann J. L., Chateigner D., and Lamble G. M. (2000) Quantitative Zn speciation in smelter-contaminated soils by EXAFS spectroscopy. *Am. J. Sci.* **300,** 289–343.

Manceau A. and Schlegel M. L. (2001) Texture effect on polarized EXAFS amplitude. *Phys. Chem. Miner.* **28,** 52–56.

Matocha C. J., Elzinga E. J., and Sparks D. L. (2001) Reactivity of Pb(II) at the Mn(III,IV) (oxyhydr)oxide-water interface. *Environ. Sci. Technol.* **35,** 2967–2972.

Morin G., Ostergren J. D., Juillot F., Ildefonse P., Calas G., and Brown G. E. (1999) XAFS determination of the chemical form of lead in smelter-contaminated soils and mine tailings: Importance of adsorption processes. *Am. Miner.* **84,** 420–434.

O'Day P. A., Rehr J. J., Zabinsky S. I., and Brown Jr. G. E. (1994) Extended X-ray absorption fine structure (EXAFS) analysis of disorder and multiple-scattering in complex crystalline solids. *J. Am. Chem. Soc.* **116,** 2938–2949.

Ostergren J. D., Brown Jr. Parks G. A. G. E., and Tingle T. N. (1999) Quantitative lead speciation in selected mine tailings from Leadville, CO. *Environ. Sci. Technol.* **33,** 1627–1636.

Post J. E. (1999) Manganese oxide minerals: Crystal structures and economic and environmental significance. *Proc. Nat. Acad. Sci. USA* **96,** 3447–3454.

Post J. E. and Appleman D. E. (1988) Chalcophanite $ZnMn_3O_7{\cdot}3H_2O$: New crystal-structure determination. *Am. Miner.* **73,** 1401–1404.

Rehr J. J., Mustre de Leon J., Zabinsky S. I., and Albers R. C. (1991) Theoretical X-ray absorption fine structure standards. *J. Am. Chem. Soc.* **113,** 5135–5145.

Ross S. J., Franzmeier D. P., and Roth C. B. (1976) Mineralogy and chemistry of manganese oxides in some Indiana soils. *Soil Sci. Soc. Am. J.* **40,** 137–143.

Rouse R. C. (1971) The crystal structure of quenselite. *Zeit. Krist.* **134,** 321–332.

Sahl K (1974) Verfeinerung der kristallstruktur von cerussit, $PbCO_3$. *Zeit. Krist.* **139,** 215–222.

Sarret G., Manceau A., Spadini L., Roux J. C., Hazemann J. L., Soldo Y., Eybert-Bérard L., and Menthonnex J. J. (1998) Structural determination of Zn and Pb binding sites in Penicillium chrysogenum cell wall by EXAFS spectroscopy. *Environ. Sci. Technol.* **32,** 1648–1655.

Shannon R. D. and Prewitt C. T. (1969) Effective ionic radii in oxides and fluorides. *Acta Cryst.* **B25,** 925–945.

Silvester E., Manceau A., and Drits V. A. (1997) The structure of synthetic monoclinic Na-rich birnessite and hexagonal birnessite. Part 2. Results from chemical studies and EXAFS spectroscopy. *Am. Mineral.* **82,** 962–978.

Stern E. A. (1993) Number of relevant independent points in X-ray–absorption fine-structure spectra. *Phys. Rev.* **B48,** 9825–9827.

Strobel P., Durr J., Tuilier M. H., and Charenton J. C. (1993) Extended X-ray absorption fine structure study of potassium and caesium phyllomanganates. *J. Mater. Chem.* **3,** 453–458.

Taylor R. M., McKenzie R. M., and Norrish K. (1964) The mineralogy and chemistry of manganese in some Australian soils. *Aust. J. Soil Res.* **2,** 235–248.

Taylor R. M., McKenzie R. M., Fordham A. W., and Gillman G. P. (1983) Oxide minerals. *Soils: An Australian Viewpoint*. Sponsored by the Division of Soils, Commonwealth Scientific and Industrial Research Organization, Australia; CSIRO, London: Academic Press.

Teo B. K. (1986) *EXAFS: Basic Principles and Data Analysis*. Springer-Verlag.

Töpfer J., Trari M., Gravereau P., Chaminade J. P., and Doumerc J. P. (1995) Crystal growth and reinvestigation of the crystal structure of crednerite, $CuMnO_2$. *Zeit. Krist.* **210,** 184–187.

Usui A. (1979) Nickel and copper accumulations as essential elements in 10-Å manganite of deep-sea manganese nodules. *Nature* **279,** 411–413.

Uzochukwu G. A. and Dixon J. B. (1986) Manganese oxide minerals in nodules of two soils of Texas and Alabama. *Soil Sci. Soc. Am. J.* **50,** 1358–1363.

Wadsley A. D. (1955) The crystal structure of chalcophanite, $ZnMn_3O_7{\cdot}3H_2O$. *Acta Cryst.* **8,** 1165–1172.